Sustainable Cities and Society 130 (2025) 106498

Contents lists available at ScienceDirect

Sustainable Cities and Society

journal homepage: www.elsevier.com/locate/scs

District-scale cumulative heat stress mapping using very-high-resolution spatiotemporal simulation

Nicola Colaninno [a,*], Agnese Salvati [b], Judit Lopez-Besora [b], Michele Morganti [c]

[a] *Department of Architecture and Urban Studies (DAStU), Politecnico di Milano, Milan, Italy*
[b] *Architecture, Energy and Environment (AiEM), Barcelona School of Architecture, Universitat Politècnica de Catalunya·Barcelona Tech - UPC, Barcelona, Spain*
[c] *SOS Urban Lab - DICEA Department, Sapienza University of Rome, Italy*

ARTICLE INFO

Keywords:
Heat stress
Urban climate
Urban morphology
Tree canopy
Microclimate simulation
SOLWEIG

ABSTRACT

Urban heat stress is a pressing issue, intensified by climate change and urban heat islands. This study introduces a methodology for creating very-high-resolution districtscale cumulative heat stress maps to support climate-responsive urban planning. Using the SOLWEIG model, we simulated mean radiant temperature (Tmrt) across Barcelona’s Gràcia district, achieving high accuracy by employing an anisotropic sky model and a 10 % tree canopy transmissivity coefficient. Simulations for the hottest day of 2022 revealed significant variations in outdoor heat stress due to urban morphology and vegetation. Analysis of three plazas and four urban canyons with differing designs and vegetation levels demonstrated that tree cover can reduce peak Tmrt by over 20 °C in exposed areas. Hourly Tmrt maps enabled the creation of a novel district-scale cumulative heat stress map, highlighting daily hours of extreme heat stress and revealing hotspots and cooler zones shaped by urban geometry and tree cover. These findings underscore the critical role of vegetation and urban design in mitigating heat stress and enhancing thermal comfort. The study provides actionable insights for city planners, practitioners, and policymakers to reduce health risks from extreme heat, fostering urban resilience and sustainability amidst global warming.

1. Introduction

In the era of climate change, cities are facing escalating environmental challenges. Rising global temperatures and increasingly intense and frequent heatwaves impose a substantial burden on the built environment, straining public spaces, infrastructure, and buildings, while also posing significant risks to human well-being and health (Bobb et al., 2014; Glazer, 2005; Lin et al., 2009; Linares et al., 2020; Schapiro et al., 2024; World Health Organization & UN-Habitat, 2016).

Extreme temperatures disproportionately affect urban populations, primarily due to the urban heat island (UHI) effect. This phenomenon occurs when heat-absorbing surfaces, high-density development, and human-generated heat intensify temperature spikes, increasing the risk of overheating (Salamanca et al., 2014; Salvati et al., 2022; Steemers et al., 1998; Stewart & Oke, 2012).

In this context, urban features such as geometry, materials, and vegetation, play a key role in shaping the microclimate and determining outdoor thermal comfort (OTC) (Lau et al., 2015; Lindberg & Grimmond, 2011). These features influence evapotranspiration, shading, and the thermal and radiative properties of surfaces, such as emissivity and albedo, and modify the shortwave radiation incident on the body as well as long-wave exchanges with the environment (Emmanuel & Fernando, 2007; Erell et al., 2012; Evola et al., 2021; Mayer et al., 2008; Salvati et al., 2022).

Numerous studies have examined the impact of key urban features on street-level microclimate (Krayenhoff et al., 2021), including urban morphology and sky view factor (L. Chen et al., 2012; Dirksen et al., 2019; Unger, 2004), tree canopy cover (Georgi & Dimitriou, 2010; Oliveira et al., 2011; Shashua-Bar et al., 2011; Streiling & Matzarakis, 2003), and urban materials (Alchapar et al., 2014; Barišić et al., 2022; Erell et al., 2014; Jandaghian & Akbari, 2018; Lindberg et al., 2016; Mohammad et al., 2021). Trees, in particular, have emerged as powerful allies in mitigating daytime outdoor heat stress, primarily through evapotranspiration and shade (Konarska et al., 2014; Lee et al., 2020; Palme et al., 2020).

On the one hand, Studies have explored methodologies to map heat exposure across urban areas using satellite thermal imagery to capture land surface temperature (Elmarakby & Elkadi, 2024; Inostroza et al.,

---

* Corresponding author at: Via Edoardo Bonardi, 3, 20133 Milano MI, Italy.
E-mail address: nicola.colaninno@polimi.it (N. Colaninno).

https://doi.org/10.1016/j.scs.2025.106498
Received 6 December 2024; Received in revised form 29 April 2025; Accepted 27 May 2025

2016; Nichol & To, 2012; Pappalardo et al., 2023). While this approach provides an overview of city-scale temperature differences, it lacks the resolution needed to assess microclimate variability and thermal sensation in different urban spaces (Villaverde et al., 2024). Additionally, the temporal limitations of thermal satellite imagery hinder analysis of hourly heat stress fluctuations.

On the other hand, to overcome these limitations and generate detailed spatial and temporal microclimate data, numerical simulations are used for OTC analysis, though at a high computational cost (Huang et al., 2024). Common models include Rayman, ENVI-met, UMEP--SOLWEIG, and the Ladybug tools suite. However, many studies focus on simplified urban forms (Nazarian et al., 2017, 2019), isolated street canyons, or overlook the impact of tree canopies on outdoor conditions (Aghamolaei et al., 2020; Evola et al., 2020, 2021). Despite advancements in simulation tools, a gap remains in metrics for assessing comprehensive urban heat exposure and its temporal variability.

This study addresses these limitations by advancing a methodology to map heat stress through very-high-resolution microclimate simulations that integrate both spatial and temporal aspects of urban heat hazard. While not exhaustive, this approach marks a significant step toward more detailed, context-sensitive assessments of urban thermal stress.

To our knowledge, current research still faces challenges in providing scalable, high-resolution tools for urban planners to assess cumulative heat exposure over an entire day across large urban areas in realistic scenarios. As a result, significant barriers remain in transforming microclimate analysis into actionable, climate-responsive urban planning and design strategies.

This study aims to develop a replicable methodology for district-scale cumulative heat stress assessment. Unlike studies that focus on single-time evaluations or simplified geometries, our approach is novel in the following ways:

- High-Resolution Simulation: Using SOLWEIG, the hourly mean radiant temperature (T_{mrt}) is modeled at a 1-meter resolution, providing detailed spatial and temporal insights into microclimate dynamics.
- Field-Driven Parameter Refinement: Field measurements refine key parameters (e.g., tree canopy transmissivity, sky model selection), ensuring alignment with the study area's unique conditions and enhancing the reliability of input data for high-resolution modeling.
- Cumulative Heat Stress Mapping: Hourly T_{mrt} simulations are aggregated into a novel heat stress metric, identifying persistent hotspots where extreme heat thresholds are exceeded over extended durations, filling a key gap in time-resolved heat risk assessments.

The paper is structured as follows: we begin with a review of current measurement techniques, microclimate simulation methods, and approaches for cumulative heat stress analysis. Next, the study area is introduced, followed by a description of a microclimate measurement campaign across three plazas and district-level modeling. Model sensitivity to key parameters, such as tree canopy transmissivity and sky model, is examined through comparison with on-site measurements. Results are presented comparing model outputs with observational data, analyzing spatial and temporal heat stress variations on a typical hot day, and the influence of urban geometry, sky model, and trees. Finally, we develop a replicable cumulative heat stress map and discuss its implications for climate-sensitive urban planning.

2. Literature review

2.1. Outdoor thermal comfort: measuring and modeling

Mean radiant temperature (T_{mrt}) is a key variable influencing human thermal comfort in outdoor environments, with its spatial and temporal variability closely tied to urban morphology, including geometry, tree cover, and surface materials. Defined as the uniform temperature of an imaginary enclosure where the radiant energy exchanged with the human body matches that in the actual outdoor environment, T_{mrt} reflects the dynamic interaction of urban elements with shortwave (direct, diffuse, and reflected) and longwave radiation fluxes. It provides a reliable measure of OTC in both sunny and shaded conditions (Lindberg et al., 2008; Matzarakis et al., 2007, 2010).

Despite the use of advanced thermal comfort indices such as the Physiologically Equivalent Temperature (PET) and the Universal Thermal Climate Index (UTCI) to assess human thermal perception, T_{mrt} remains widely recognized as a key determinant of thermal perception in outdoor environments (Gál & Kántor, 2020; Lindberg et al., 2008; Staiger & Matzarakis, 2020; Thorsson et al., 2007). Research has demonstrated a strong correlation between T_{mrt} and both UTCI and PET values (Mahdavinejad et al., 2024). However, evaluating T_{mrt} experimentally in outdoor settings remains particularly challenging (Banfi et al., 2022; Johansson et al., 2014).

Among the most accurate methods for measuring T_{mrt} is the use of integral radiation measurements through three net radiometers (Banfi et al., 2022; Höppe, 1992; Thorsson et al., 2007). This approach allows for a comprehensive capture of the radiant energy exchange, contributing to a more precise computation of T_{mrt}. However, the high cost of these sensors can limit their large-scale application.

Alternative methods have been explored for their affordability and accessibility, despite limitations. One such approach involves using a single pyranometer and pyrgeometer mounted on movable axes oriented in six directions (Kántor et al., 2012, 2012; Oliveira et al., 2011; Vanos et al., 2021). This method is simpler and more cost-effective than using three net radiometers. Moreover, using globe thermometers combined with air temperature and wind speed measurements is a widely recognized yet simplified approach (Banfi et al., 2022; Dear, 1988; Johansson et al., 2014; Spagnolo & de Dear, 2003; Teitelbaum et al., 2022; Thorsson et al., 2007; Vernon & Warner, 1932). While more affordable and commonly used indoors, its accuracy in outdoor urban settings remains under investigation (Banfi et al., 2022).

Overcoming such restrictions has increasingly promoted the exploration of various computer techniques for simulating T_{mrt}. Currently, a handful of robust tools are prominent in this domain, including the SOlar LongWave Environmental Irradiance Geometry (SOLWEIG) model (Bäcklin et al., 2021; Briegel et al., 2023; Lau et al., 2015, 2022; Li, 2021; Lindberg et al., 2008; Mutani & Beltramino, 2022; Thorsson et al., 2017), ENVI-met (Bruse & Fleer, 1998; Emmanuel & Fernando, 2007), RayMan (Krüger et al., 2012; Matzarakis et al., 2007, 2010), or the Ladybug Tools suite within Grasshopper (Roudsari & Pak, 2013).

The radiation and human-bioclimate model RayMan is among the most recognized tools, allowing effective simulation of short- and long-wave radiation flux densities from three-dimensional surroundings in simple and complex environments. However, calculations are made for single points. This limitation is overcome by ENVI-met, Ladybug, and the SOLWEIG model, which allow the spatial computation of T_{mrt} over uniform gridded surfaces (Aleksandrowicz et al., 2020) or using 3D models.

ENVI-met is a three-dimensional non-hydrostatic proprietary simulation tool for effective micro-scale computational fluid dynamics (CFD) modeling. ENVI-met has some critical restrictions, such as the need for site-specific meteorological data for appropriate initialization, the extensive computation time for simulating even a small region, and the constraints of the orthogonal grid for 3D modeling within the software environment (Aleksandrowicz et al., 2020).

While the Ladybug tools suite is widely recognized for its versatility and widespread adoption in environmental analysis for evidence-based design, both at the building and urban scale, it also comes with certain limitations when the objective is simulating over extensive areas. In Ladybug, long-wave radiation T_{mrt} is based on the Honeybee/Energyplus surface temperatures simulation, while short-wave radiation is computed using the Ladybug SolarCal module. Therefore, 3D models featuring complex geometries or extensive datasets may demand substantial computational resources due to their inherent complexity (Evola et al., 2020).

SOLWEIG model is an open-source GIS-based tool currently available through the Urban Multi-scale Environmental Predictor (UMEP), a comprehensive tool for city-based climate analysis integrated into the open-source GIS platform QGIS. SOLWEIG has demonstrated a high-accuracy prediction of observed radiation fluxes, explaining 94 % of the variations in T_{mrt} and an overall RMSE of 4.8 K (Lindberg et al., 2008; Thorsson et al., 2017).

Studies conducted comparing RayMan, ENVI-met, and SOLWEIG report certain variability of performance and errors depending on the weather conditions, hourly variation, and latitude (Jänicke et al., 2021). However, although all three models under-estimate night-time T_{mrt}, overall, SOLWEIG showed the lowest deviations from observations (Gál & Kántor, 2020; Jänicke et al., 2021) standing as a robust, accessible, and pivotal tool for research endeavors and practical applications in various professional domains. By harnessing very-high-resolution (VHR) Digital Elevation Models (DEMs) as input, SOLWEIG facilitates large-scale simulations of radiation fluxes and T_{mrt} in complex urban environments. SOLWEIG is used in this study to generate high-resolution spatio-temporal T_{mrt} data for cumulative heat stress analysis and district-scale mapping.

2.2. High-resolution, time-resolved urban heat stress mapping

Recent contributions to the field have made significant progress in localized heat assessment. For instance, Weeding et al. (2024) employed SOLWEIG to project outdoor thermal stress in Tasmania for a 150 m x 150 m study site. While this is an important step toward localized heat assessment, their focus remains confined to a small area and does not capture intra-neighborhood variability or cumulative hourly exceedance metrics.

Conversely, Chakraborty et al. (2019) provide a valuable analysis of urban heat at the neighborhood level, but their use of low-resolution 1 Km LST lacks the biophysical comprehensiveness of T_{mrt} and the needed urban details of microclimate simulation. Wang et al. (2023) integrate machine learning and low-cost sensors to map urban heat exposure at 10-meter resolution, with their metrics primarily reflecting relative humidity and air temperature. We address these limitations by simulating VHR 1-m hourly T_{mrt} to quantify cumulative heat stress through an extremely hot day.

Studies like Diz-Mellado et al. (2021) confirm the relevance of microclimate outdoor thermal patterns using Support Vector Regression (SVR) method to predict the measured temperature inside courtyards. However, 22 selected courtyards are assessed. Our work builds on this by designing a VHR cumulative heat stress analysis across extended residential environments. This neighbor-scale emphasis, combined with detailed urban morphology (buildings, vegetation), remains underrepresented in literature.

Juzbašić et al. (2022) improved climate modeling by providing dynamic downscaling to capture variations in climate impacts. However, the proposed model refers to regional studies. While Szűcs et al. (2014) deal with the comparison of T_{mrt} data obtained by measurement and computational simulation in a densely populated city quarter of Lisbon, the measurements were carried out in a park and the surrounding canyon streets. Neither research focused on a comprehensive neighborhood-scale analysis of heat stress.

While the analysis of cumulative heat addresses a recognized gap in the literature, prominent studies such as Perkins-Kirkpatrick and Lewis (2020) and Yang et al. (2014) have primarily focused on daily or annual cumulative metrics within regional-scale contexts. While Tam et al. (2015) recognize the relevance of improving temporal resolution, the study focuses on a day-by-day analysis that is still centered on a regional scale.

Obe et al. (2024) and Luo and Lau (2021) discuss high resolution landscape-level to regional-level assessments of heat stress, respectively, including multiple metrics, but do not capture the cumulative or hourly dynamics across heterogeneous urban contexts that our study delivers.

Su et al. (2022) establish urban day and night extreme heat wave cumulative hourly interpolation models. However, the focus is on regional land use variations, and they only consider daytime vs. night-time conditions.

Our study aligns with recent studies in the field (Ding et al., 2024; 2025) addressing the challenge of achieving city-wide thermal comfort mapping at high spatial and temporal resolutions, which requires consideration of the complex urban morphology (urban geometry and land cover) at a microscale, as well as the background meteorological factors at a larger scale. However, although cutting-edge, these studies simulate city-wide comfort metrics at a 10-m spatial resolution. Also, although they simulate microclimate on an hourly basis, no cumulative effect is considered. Although relevant, this level of detail may fail to capture fine-grained spatial variability and hourly fluctuations in outdoor heat stress under realistic scenarios.

On the other hand, Li et al. (2024), who call for urban-specific thermal risk assessments, have modeled very-high spatial resolution hourly averaged UTCI, not considering the hourly cumulative impact.

Finally, as previously mentioned, studies have focused on simplified urban geometries (Nazarian et al., 2017, 2019) and isolated street canyons, or have overlooked the tree canopies' impact on outdoor conditions (Aghamolaei et al., 2020; Evola et al., 2020, 2021).

3. Materials and methods

The methodology follows a structured workflow to assess district-scale cumulative heat stress. It begins with on-site microclimate measurements—air temperature (T_a), globe temperature (T_g), and wind speed (W_s)—at selected locations to establish reference conditions and adjust T_{mrt} simulations. Simulations using the SOLWEIG model first replicate these locations and time periods, allowing direct comparison with observed T_{mrt}. Key input parameters, such as tree canopy transmissivity and sky model type, are varied to test their influence on radiation fluxes and T_{mrt}. Hence, to capture spatial patterns, simulations are scaled up district-wide for August 14, 2022—the year's hottest day. Cumulative heat stress is then quantified by aggregating T_{mrt} over a 24-hour cycle, using a 51 °C threshold. The resulting map identifies areas where T_{mrt} exceeds this value, capturing both the intensity and duration of thermal stress.

3.1. Case study

The research focuses on the Gràcia district in Barcelona, Spain (Fig. 1-a), located in the northern part of the city and adjacent to the popular Eixample district. The area, spanning about 132.21 hectares and roughly 120,000 residents, is characterized by mid-high population density. Buildings occupy about 64 % of the urban space (Salvati et al., 2019), and the compact, homogeneous fabric provides an ideal test bed for district-scale simulations. Additionally, the neighborhood's active public spaces, amenities, and pedestrian-friendly streets highlight the importance of studying outdoor conditions during extreme heat events.

Three plazas in Gràcia (Fig. 1–b), each characterized by different levels of tree canopy cover, soil permeability, and materials, have been selected for on-site microclimate measurements: Plaza de Rovira i Trias (referred to as Rovira), Plaza d'en Joanic (Joanic), and Plaza de la Revolució (Revolució).

The three plazas are roughly similar in size but show significant differences in tree coverage and paving materials (Fig. 2). In Rovira and Revolució, the ground is primarily covered with concrete slabs, while Joanic features a sandy surface. The tree species also vary, with *Platanus x hispanica* in Rovira, *Jacaranda mimosifolia* in Revolució, and *Styphnolobium japonicum* in Joanic (Ajuntament de Barcelona, 2023).

Sky View Factor (SVF) was used to compare plaza geometries,

Fig. 1. An overview of the city of Barcelona (Fig. 1-a), and the Gràcia district (Fig. 1–b), featuring the marked locations of the three Plazas (red circles in Fig. 1–b).

Fig. 2. Street-level perspective and overview of tree species and pavement materials in the three plazas: a) Rovira, b) Revolució, and c) Joanic.

calculated at the approximate center of plazas and as an average across the entire area, with and without trees (buildings only). Without trees, SVF values at the central point in Joanic and Revolució range from 0.86 to 0.74, respectively, while the average SVF is 0.79 and 0.66. These relatively small differences are primarily due to variations in the size and shape of the plazas. However, when trees are factored in, the SVF changes dramatically. In Rovira, where the tree canopy nearly covers the entire area, the SVF drops significantly from 0.79 to 0.02 at the central point and 0.73 to 0.04 as an average value. In contrast, the SVF in Joanic and Revolució is less impacted by trees, which are mainly located on the sides. Table 1 shows key features of each plaza, including SVFs, tree cover, and ground materials, along with an aerial view of each plaza.

Table 1
Aerial view and summary of Sky View Factor (SVF) values at the approximate center of each plaza, along with the average SVF for the entire area, tree cover ratio, and predominant ground material for all three plazas.

Plaza				
Rovira		SVF: point	*Buildings*	0.79
			Buildings + Trees	0.02
		SVF: Average Plaza	*Buildings*	0.73
			Buildings + Trees	0.04
		Tree Cover	*%*	0.95
		Ground Material	*Prevailing*	Concrete slabs
Revolució		SVF: point	*Buildings*	0.74
			Buildings + Trees	0.72
		SVF: Average Plaza	*Buildings*	0.66
			Buildings + Trees	0.44
		Tree Cover	*%*	0.29
		Ground Material	*Prevailing*	Concrete slabs
Joanic		SVF: point	*Buildings*	0.86
			Buildings + Trees	0.84
		SVF: Average Plaza	*Buildings*	0.79
			Buildings + Trees	0.51
		Tree Cover	*%*	0.32
		Ground Material	*Prevailing*	Sand

3.2. On-site microclimate measurements

The three plazas were used to evaluate the impact of tree cover variation on street-level microclimate conditions. The objective was to identify T_{mrt} ranges in shaded and unshaded urban spaces within the same district. A microclimate measurement campaign was planned to compare the thermal conditions of the plazas at different times of the day. On-site values were measured near the central point of each plaza. The measured parameters include black-globe temperature (T_g), air temperature (T_a), relative humidity (RH), and wind speed (W_s). These

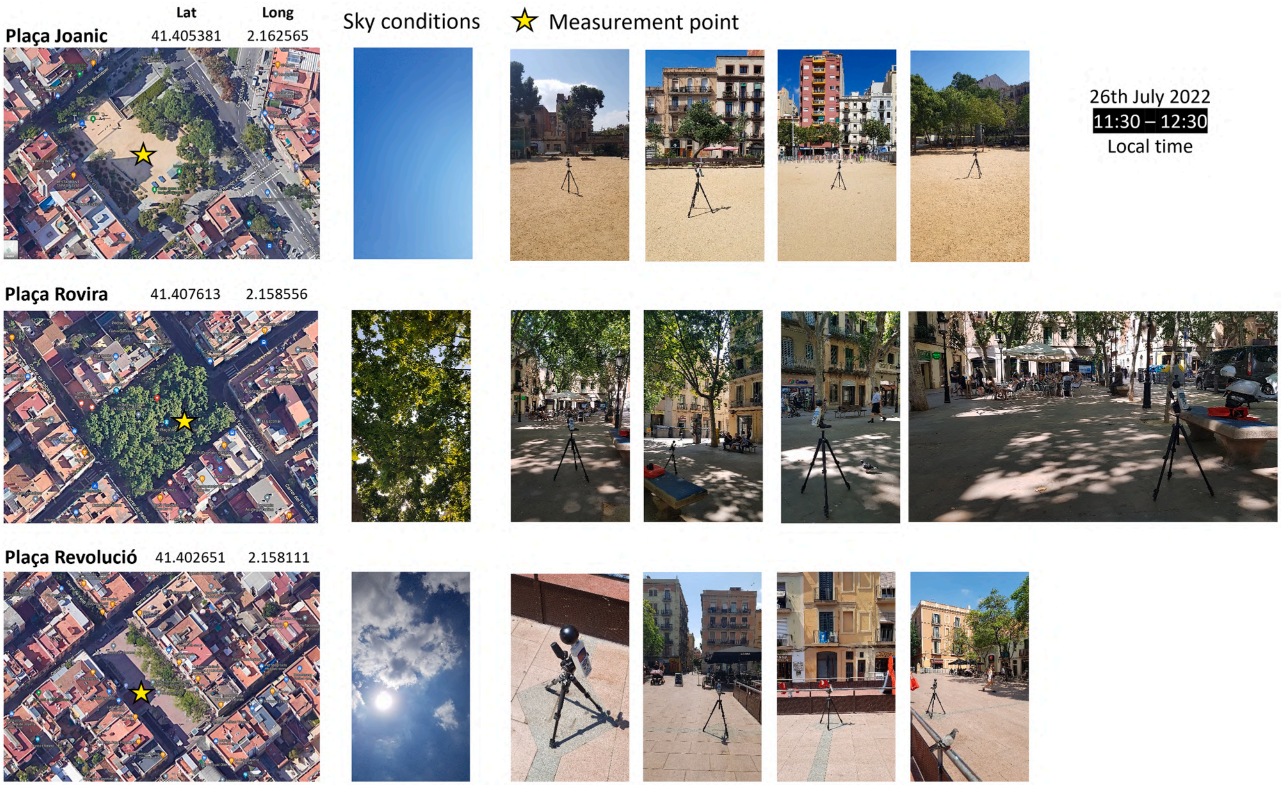

Fig. 3. Top view and street-level perspective of measurement points for each plaza, along with a view of the sky conditions at the time of the measurements.

Table 2
Specifications of the equipment employed for field measurements.

Equipment	Measured variable	Range	Accuracy
PCE-WB 20SD Environmental Meter	Black-globe Temperature	0 … +80 °C	± 0.6 °C
	Air Temperature	0 … +50 °C	± 0.6 °C
RS232 Integral Vane Digital Anemometer	Wind Speed	0.4 … 30 m/s	± (2 % of reading + 0.2 m/s)
FLIR E6-XT WiFi	Surface Temperature	−20 … +550 °C	±2 °C or ±2 % of reading for ambient temperature 10 °C to 35 °C and object temperature above 0 °C (32 °F)

were used to compute T_{mrt} at each point. To represent typical daylight summer conditions, two measurement campaigns were conducted: July 26, 2022, from 11:00 to 13:00 local time (CEST, UTC+2), to compare the thermal conditions around solar noon, and August 28, 6:00 to 7:30 local time (LT), to compare the thermal conditions in the early morning when the air temperature is minimum after nighttime cooling. As an example, Fig. 3 shows the locations and images, top- and street-view, around the measurement points for the 26th of July 2022.

Measurements were recorded in each site at one-minute intervals, over 30 min during the daytime session on July 26 and for 20 min during the early-morning session on August 28; these were conducted sequentially, beginning at Joanic, followed by Rovira, and concluding at Revolució. The environmental meter was mounted on a tripod at a height of 1.5 m above ground level. Simultaneously, a digital anemometer was used to measure wind velocity. The anemometer provided average wind speed readings, which were used to calculate T_{mrt} using T_g and T_a. Detailed specifications of the equipment used are listed in Table 2.

Measured T_a, T_g, and W_s were used to obtain street-level T_{mrt} using the ASHRAE equation (Eq. (1)), with D as the globe diameter (mm) and ε as the globe emissivity (ASHRAE, 2001).

$$T_{mrt} = \left[\left(T_g + 273.15\right)^4 + \frac{1.1 \times 10^8 \, W_s^{0.6}}{\varepsilon \, D^{0.4}} \times \left(T_g - T_a\right) \right]^{\frac{1}{4}} - 273.15 \qquad (1)$$

The ASHRAE equation has been applied in several studies investigating outdoor T_{mrt} (Johansson et al., 2014; Ng & Cheng, 2012; Thorsson et al., 2007). The factor $1.1 \times 10^8 \, W_s^{0.6}$ in the equation represents the convective heat transfer coefficient, derived empirically. Other formulations for the convective coefficient have been proposed and applied in literature (Banfi et al., 2022; Lam et al., 2018), leading to different values of T_{mrt}. Further details on temperature measurements and T_{mrt} calculations, along with discrepancies among different formulations, are provided in Annex 1, Figures A.1 and A.2.

3.3. Microclimate modeling of radiation and thermal comfort

SOLWEIG is first used to model T_{mrt} for the three plazas on the two days of the on-site campaign. The modeling was then expanded to the district level, focusing on August 14th, 2022, which was pinpointed as the peak temperature day of the year as recorded in the Raval weather station. The model was executed within the QGIS environment utilizing the UMEP plugin (Lindberg et al., 2018). The resulting data is in the form of raster maps that display the hourly spatial distribution of T_{mrt} and incoming and outgoing shortwave and longwave radiation fluxes, with a resolution of 1 m per pixel. T_{mrt} is calculated for a standing human modeled as a cylinder, using standard absorption coefficients for shortwave and longwave radiation set at 0.70 and 0.97, respectively, as detailed by (Holmer Björn et al., 2015). Additionally, hourly Physiological Equivalent Temperature (PET) is estimated for selected points.

3.3.1. Spatial data used for modeling

Modeling T_{mrt} requires VHR digital elevation models (DEMs), including digital surface models (DSM) for buildings and trees, and a digital terrain model (DTM) for the ground. We used 1-meter resolution georeferenced DSM and DTM in GeoTIFF format, projected to ETRS89/ UTM zone 31 N. These DEMs, derived from LiDAR data (XYH point clouds), were provided by the Cartographic and Geological Institute of Catalonia (ICGC) for the 2016–2017 period (Institut Cartogràfic i Geològic de Catalunya, n.d.).

SOLWEIG models trees as a separate layer for near-realistic simulations and uses the buildings' DSM to determine wall height and façade orientation (0–360°). Both DSMs are employed to estimate an advanced SVF, incorporating all view components—North, East, South, and West—along with trees. The model also integrates land cover data to account for varying albedo and emissivity across five classes: paved surfaces, buildings, grass, bare soil, and water (Lindberg et al., 2018).

For building facades, default albedo (0.20) and emissivity (0.90)

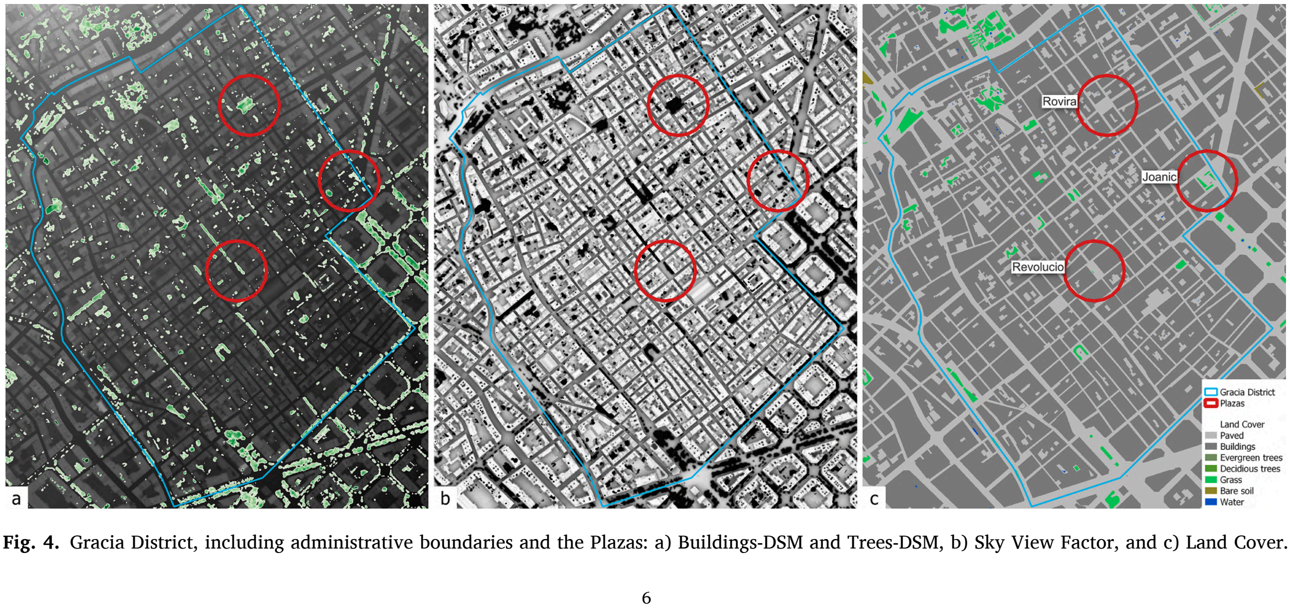

Fig. 4. Gracia District, including administrative boundaries and the Plazas: a) Buildings-DSM and Trees-DSM, b) Sky View Factor, and c) Land Cover.

values are applied district-wide. Fig. 4 presents a top-down view of the primary input data for radiation and T_{mrt} modeling in Gracia, including the DSM, buildings, trees, SVF, and land cover, with plazas highlighted for reference.

3.3.2. *Weather data sourcing and adjustment*

The weather file used for modeling includes hourly data for T_a, RH, W_s, and solar radiation (global, direct, and diffuse). This data was sourced from the Raval weather station, operated by the Meteorological Service of Catalunya (METEOCAT), which records measurements every 30 min. The station was selected for its representative location within the urban environment. A previous study (Salvati et al., 2017) found that temperatures in Gracia closely matched those recorded at the Raval station.

Since the weather station provides only global horizontal irradiation (GHI), the Boland-Ridley model (Boland et al., 2008) was used to derive the direct and diffuse components of solar irradiation from the GHI. Additionally, because wind speed is measured at 10 m height, the power law equation (Eq. (2)) was used to derive wind speed at 1.5 m above ground level (agl) (Salvati et al., 2020).

$$\frac{V}{V_m} = kZ^{\alpha} \tag{2}$$

Where V is the mean W_s (m/s) at a given height, Z is the anticipated height (equal to 1.5 m agl in our study), and V_m is the wind speed at the meteorological station. k and α are coefficients that depend on the terrain roughness, as reported in (Salvati et al., 2020). We used the values corresponding to an urban terrain, namely 0,35 for k and 0,25 for α. In Annex 2 of supplementary material, Figure A.4 reports the 24-hour weather values employed for the simulations in this study, encompassing GHI, T_a, RH, and W_s. Figure A.5 of Annex 2 shows the impact of an adjusted W_s height on thermal comfort estimation.

3.3.3. *Tree canopy transmissivity*

Trees DSM serves as the input for the tree canopy cover, adhering to the vegetation scheme outlined by (Lindberg & Grimmond, 2011). Two key parameters are required for modeling radiation and T_{mrt}: solar transmissivity of the foliage (τ_I), which indicates the proportion of direct solar radiation that passes through the tree crown, and the percentage of trunk height relative to the total tree height. The latter is empirically set at 25 %. Tree solar transmissivity holds substantial influence as it notably diminishes the global incident radiation reaching the ground, thus affecting T_{mrt}.

In SOLWEIG, the default value of τ_I is set to 3 %. This value is based on research that represents the average transmissivity measurements for common urban tree species in northern Europe (Konarska et al., 2014). However, the observed species are not prevalent in Barcelona. Additionally, this value is representative of single urban trees. The transmissivity of direct solar radiation through single trees tends to be lower compared to forest canopies due to the latter's inherent heterogeneity, including gaps between trees and less dense crowns than individual trees (Konarska et al., 2014). Transmissivity of direct solar radiation through the crowns of trees organized in adjacent rows, such as those in Rovira, is expected to be greater than 3 %.

The solar transmissivity of the Platanus species, found in Rovira, prevalent in many tree-lined streets in Barcelona, has been examined in other cities with a Mediterranean climate, yielding values of approximately 10–12 % (Cantón et al., 1994; Palme et al., 2020). These studies also indicate even higher solar transmissivity factors for species characterized by less homogeneous and dense crowns. Drawing from this literature, we have tested three distinct values of τ_I, namely, 3, 10, and 20 %, as reported in Table 3.

3.3.4. *Fine-tuning input parameter: transmissivity and sky model*

Before scaling up T_{mrt} to the district level, we simulated radiation and T_{mrt} for the three plazas, using data from the campaign days—July 26 (11:00 to 13:00 LT) and August 28 (6:00 to 7:30 LT). This step was crucial for fine-tuning the input parameters. We specifically evaluated the impact of three different tree canopy transmissivity values, each tested with the isotropic and the anisotropic sky model. The anisotropic sky model is particularly relevant as it accounts for variations in incoming diffuse shortwave and longwave radiation fluxes based on the zenith angle (Wallenberg et al., 2020, 2023).

This resulted in six different scenarios (Table 4), combining three transmissivity levels—3 %, 10 %, and 20 %—with both isotropic (s1, s2, s3) and anisotropic (s4, s5, s6) sky. We then compared the SOLWEIG-generated maps with on-site T_{mrt} values. Additionally, we assessed the model's sensitivity across the six scenarios in terms of estimated shortwave and longwave radiant fluxes.

4. Results

4.1. *Observed microclimate variations: analysis and insights*

A comparison between recorded T_a and T_g, and the resulting T_{mrt} according to the ASHRAE equation, is first presented. Fig. 5 shows the average values for the campaign days and hours for each plaza. The recorded 1-min T_g values showed large fluctuations due to rapid changes in radiation fluxes and wind speed, which is typical of outdoor settings. To reduce such fluctuations, we considered the average value of T_{mrt} over the measurement period. This is the suggested approach to reduce the scattering of T_{mrt} values based on black-globe thermometer measurements (Banfi et al., 2022).

The average T_{mrt} values are calculated as the mean of the 1-min values over a measurement period, discarding the first 10 min needed for the globe thermometer to reach thermal equilibrium. Detailed 1-minute measurement data is provided in Figure A.1 of Annex 1 in the supplementary material.

On the 26th of July, around noon, evident variations in T_g are observed among the three plazas. Notably, T_g is remarkably lower in Rovira than the other two plazas, attributed to the favorable influence of tree shading. In Rovira, T_g (30.3 °C) closely reflects the air temperature (29.9 °C) due to the attenuation of direct solar radiation flux by the tree canopy. Conversely, significant differences between T_g and T_a were found in the other two plazas. In Joanic, measured T_g was 43.1 °C, being 11.0 °C higher than T_a (32.1 °C). In Revolució, the measured T_g was 41.9 °C, which was 9.2 °C higher than air temperature (32.7 °C). Also, Plaza Rovira exhibited lower T_a, being 2.2 °C cooler than Joanic and up to 2.8 °C cooler than Revolució.

The data collected on August 28th showed lower overall

Table 3
Transmissivity values of light through the tree foliage tested in this study as parameters used in the SOLWEIG model.

Tree species and arrangement	Transmissivity (τ_I)	Reference study
Single (urban) tree Dense crown, typical of northern Europe	3 %	Konarska et al. (2014)
Trees arranged in adjacent rows Reference species: Platanus	10 %	Palme et al. (2020) Cantón et al. (1994)
Non-homogenous crowns, arranged in row Reference species: Pinus	20 %	Palme et al. (2020)

Table 4
Summary of simulation scenarios (s1-s6) with different sky models and tree solar transmissivity.

	s1	s2	s3	s4	s5	s6
Sky Model	Isotropic	Isotropic	Isotropic	Anisotropic	Anisotropic	Anisotropic
Tree Canopy Solar Transmissivity	$\tau_I = 3$ %	$\tau_I = 10$ %	$\tau_I = 20$ %	$\tau_I = 3$ %	$\tau_I = 10$ %	$\tau_I = 20$ %

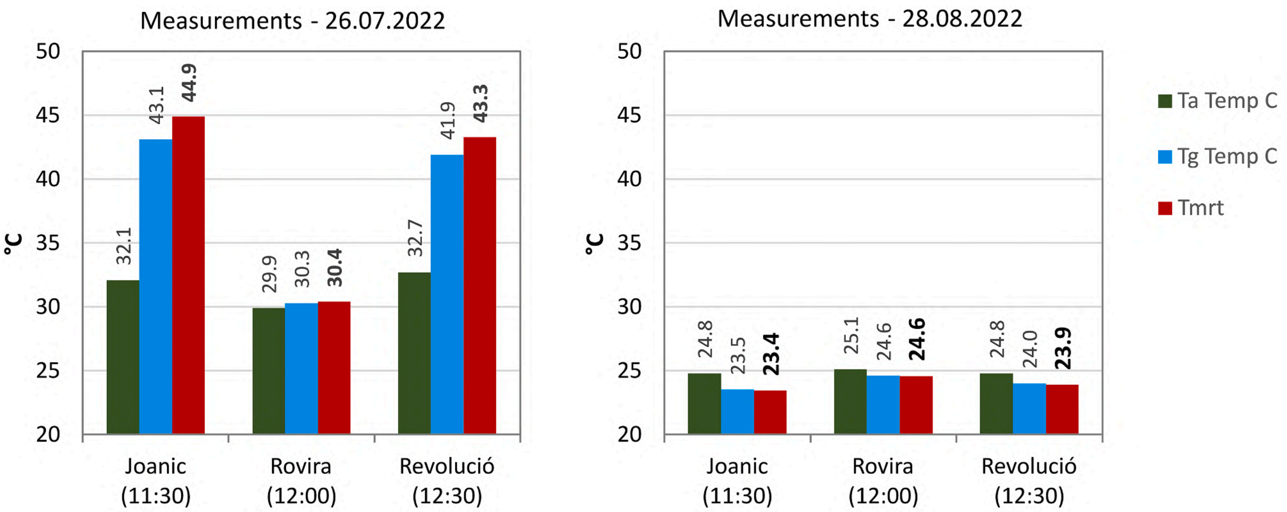

Fig. 5. Average recorded T_a and T_g values for the two days of the campaign and the corresponding T_{mrt}.

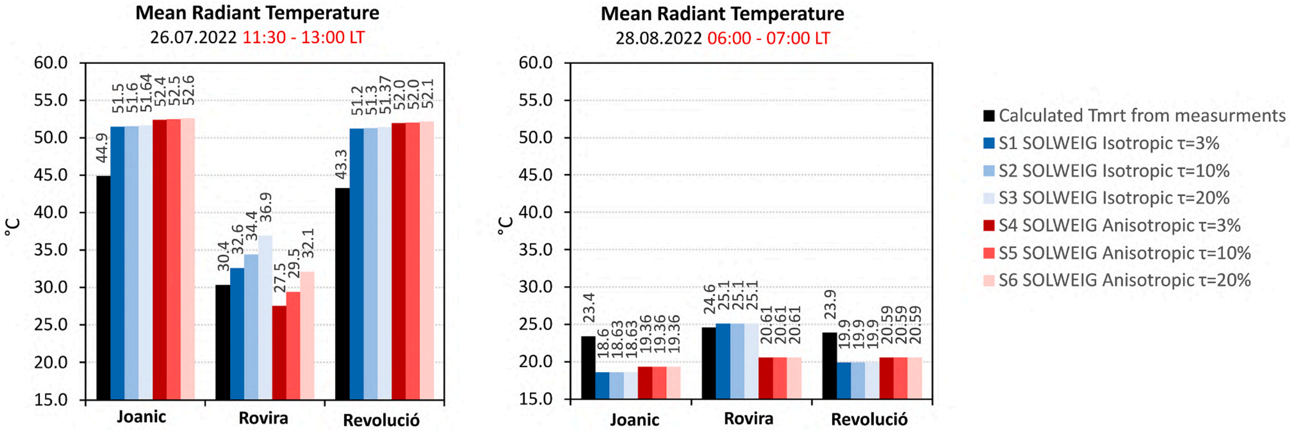

Fig. 6. Comparison of SOLWEIG simulation results (s1-s6) with on-site T_{mrt} measurements for the two campaign days: July 26, 2022 (11:30–13:00 LT) and August 28, 2022 (06:00–07:00 LT).

temperatures and a reduced variation between T_a and T_g across the three plazas compared to July 26th. This likely results from the early morning timing of the measurements (7:15 a.m.), coinciding with lower surface temperatures after nighttime cooling. As a result, T_g showed less fluctuation and was closer to T_a at all three sites.

On the 28th in Rovira, both T_a and T_g were slightly higher. This can be attributed to the dense tree cover, which reduces the SVF and limits night-time longwave radiation loss from horizontal surfaces. The tree canopy also affects wind speed and convective heat transfer, leading to warmer ground and façades during nighttime and early morning hours, as observed in this case, compared to the other two plazas. Similar observations have been reported for the city of Mendoza (Correa et al., 2012). To gain a deeper understanding of these dynamics, we also used a thermal infrared camera to capture radiant temperatures of the ground, walls, and sky during the two measurement periods (see Annex 1 – Fig. A.3).

On July 26th, T_{mrt} (30,4 °C) in Rovira closely aligns with T_g (30.3 °C). This close correlation is due to the tree canopy's shading effect, which reduces the SVF and the low average wind speed of 0.6 m/s during measurements.

Joanic and Revolució, which have higher SVF values, showed much higher T_{mrt} than Rovira. T_{mrt} was 44.9 °C in Joanic and 43.3 °C in Revolució, values that are slightly higher than the measured T_g due to the convective heat transfer induced by wind speed, whose average value over the measurement period was 1 m/s and 1.1 m/s in Joanic and Revolución, respectively.

On August 28th, T_{mrt} closely matched T_g across all observations. This observation aligns with the environmental conditions at the time of the observations, including the absence of direct solar radiation and cooler surrounding surfaces compared to the air temperature.

4.2. Comparison of modeled and on-site measured values

Through comparing SOLWEIG outputs with field-based T_{mrt}, we first aim to qualitatively assess the model's ability to estimate T_{mrt} in different conditions of shortwave and longwave radiation fluxes in our study area. Hence, the measurements are used as a reference to understand the impact of two key parameters, i.e., the tree canopy transmission coefficient and the sky model type (isotropic vs. anisotropic). Six simulations (s1–s6) were conducted (see Table 4, Section 2.3.4). Fig. 6 compares SOLWEIG results and on-site T_{mrt} measurements. Input weather data and outputs of the SOLWEIG simulations have a hourly resolution. For the comparison, we used the output value of the closest time to the actual measurement period. A maximum time difference of about 30 min between the measured and the simulated values exists.

The results from July 26th are particularly effective for assessing simulated T_{mrt} at points exposed to direct solar radiation as opposed to points with shaded conditions.

At locations with direct sun exposure, i.e. Revolució and Joanic, the T_{mrt} estimated by SOLWEIG is higher than the measurement-based values. The overestimation varies between + 6.6 °C and +8.7 °C. Results for Revolució exhibit considerable similarity with Joanic. Since nearby trees do not shade these points, the simulation results are unaffected by variations in tree solar transmissivity. In such locations characterized by high SVF, employing the anisotropic sky model yields slightly higher T_{mrt} values (+0.9–1.0 °C) than those utilizing the isotropic sky model. Conversely, at shaded points beneath the tree canopy (Rovira), T_{mrt} estimated using the anisotropic sky model is 4.8 to 5.1 °C lower than when using the isotropic model.

At shaded locations, the isotropic sky model overestimates T_{mrt} compared to the measured value. Conversely, the anisotropic model returns values closer to the field measurements, with variation above and below depending on the tree canopy solar transmissivity. The best T_{mrt} estimate is achieved with the anisotropic sky and tree solar transmissivity of 10 %, which yielded a simulated value of 29.5 °C compared to the measured value of 30.4 °C.

The relative increase in T_{mrt} for escalating values of tree canopy transmissivity remains consistent across both sky models.

The results for August 28 show reduced variability across simulation settings, as the early morning timing minimized the influence of tree solar transmissivity due to the lack of direct solar radiation. Instead, the anisotropic sky model's effect persisted, lowering T_{mrt} by approximately 4.5 °C under tree canopies and increasing it by around 0.7 °C in areas with high SVF, such as Joanic and Revolució. Overall, in this time frame, using an anisotropic sky model consistently shows lower T_{mrt} values compared to the measurement-based T_{mrt} by 3.3 – 4.0 °C across all three sites. Conversely, when employing the isotropic model, T_{mrt} is underestimated by 4.0 - 4.8 °C for locations with high SVF and slightly overestimated (+0.5 °C) for points situated beneath the tree canopy, such as Rovira.

The comparison between simulations and measurements confirms that T_{mrt} trends are largely influenced by sky openness and solar exposure. It also confirms the relevance of sky model type and tree solar transmissivity on the T_{mrt} estimate, especially for points under trees. For shaded areas with significant tree cover (e.g., Rovira), the anisotropic sky model with 10 % tree canopy transmissivity is the best combination, returning T_{mrt} values that closely match on-site measurements for the studied points. In early morning conditions, with lower solar radiation, the anisotropic model still performs better, although the variability between the two models is less pronounced. At exposed locations, the T_{mrt} results are much less affected by sky model choice and tree solar transmissivity coefficient.

4.3. SOLWEIG model sensitivity across study sites

This section observes the SOLWEIG model sensitivity across our study sites, focusing on diurnal variation, sky model settings, and canopy transmissivity. Given that temperatures were higher on August 28th than on July 26th, we used the August 28th simulations to examine how different sky models and tree canopy transmissivities affect shortwave and longwave radiation, as well as T_{mrt}. Fig. 7 compares radiation fluxes for two representative locations: Joanic, with a high SVF, and Rovira, characterized by low SVF due to extensive tree cover.

In Joanic, results indicate that the anisotropic sky model (red lines) yields slightly lower values of incoming shortwave radiation. The maximum absolute difference observed is a reduction of 46.8 W/m^2 at 14:00, approximately 10 % less than the incoming radiation calculated by the isotropic model. Findings for Rovira highlight the substantial impact of varying tree transmissivity on the incoming radiation beneath the trees' canopy. Changing tree canopy transmissivity from 3 % to 10 % increases the maximum incoming shortwave radiation from 52.4 W/m^2 to 97.9 W/m^2, representing an increase of 84 %. Further increasing transmissivity from 10 % to 20 % results in a maximum incoming shortwave radiation of 162.9 W/m^2, a 211 % increase from the 3 % transmissivity case.

Conversely, the choice between isotropic and anisotropic sky models has a relatively minor effect on incoming shortwave radiation beneath tree canopies. Interestingly, the maximum observed difference occurs at 20 % tree transmissivity, where the anisotropic sky model predicts 7.4 W/m^2 less incoming shortwave radiation compared to the isotropic model, a reduction of about 4 %. This highlights that the sky model's effect on incoming solar radiation becomes more pronounced with increased solar exposure. The anisotropic sky model consistently predicts slightly lower values at both locations for incoming longwave radiation. The difference is modest and remains relatively stable throughout the day.

While the sky model does not affect outgoing longwave radiation, tree canopy transmissivity does have an impact at shaded locations like Rovira. Increasing tree transmissivity from 3 % to 20 % results in a rise of up to 22.8 W/m^2 in outgoing longwave radiation at noon, representing a 5 % increase. However, this effect is relatively minor during nighttime. Fig. 8 illustrates the daily variation in T_{mrt}, highlighting the influence of both the sky model and tree transmissivity. These factors have a considerable effect on T_{mrt} in shaded areas like Rovira but are less impactful in locations with high SVF, such as Joanic.

In Rovira, the anisotropic sky model consistently produces lower T_{mrt} values throughout the day. The reduction is 4.5 °C during nighttime and up to 5 °C during daytime hours. In Joanic, the use of an anisotropic sky model compared to the isotropic one returns a small increase in T_{mrt}, reaching up to 1.3 °C for the nighttime estimations.

This can be explained by how the anisotropic model adjusts sky emissivity according to varying zenith angles, which affects the radiant load on a person in areas with high SVF, such as Joanic. High exposure to the warm sky (high emissivity) at high zenith angles results in increased T_{mrt} compared to a uniform sky model. These findings align with previous research (Wallenberg et al., 2020, 2023).

In Rovira, transmissivity significantly influences T_{mrt} calculations, with similar trends observed using both isotropic and anisotropic sky models. The most significant impact on T_{mrt} occurs at the daily peak around 13:00. Increasing tree solar transmissivity from 3 % to 10 % raises T_{mrt} by approximately 2.5 °C and up to 6 °C when transmissivity is increased to 20 %. Figure A.6 in Annex 3 summarizes the effects of isotropic and anisotropic sky models and tree solar transmissivity on T_{mrt} at two locations: Joanic (high SVF) and Rovira (low SVF). Overall, both the sky model and tree canopy transmissivity are crucial factors influencing SOLWEIG's radiation flux and T_{mrt} predictions, especially in low-SVF areas, under tree cover.

4.4. District-scale mean radiant temperature and thermal comfort

With a well-defined frame for the input parameters, we modeled district-scale, very high-resolution (VHR) hourly T_{mrt} for August 14th, 2022, identified as the hottest day of the year based on data from the Raval weather station (see Fig. A.7, Annex 4). The T_{mrt} was simulated using an anisotropic sky model and a tree canopy solar transmissivity of 10 %.

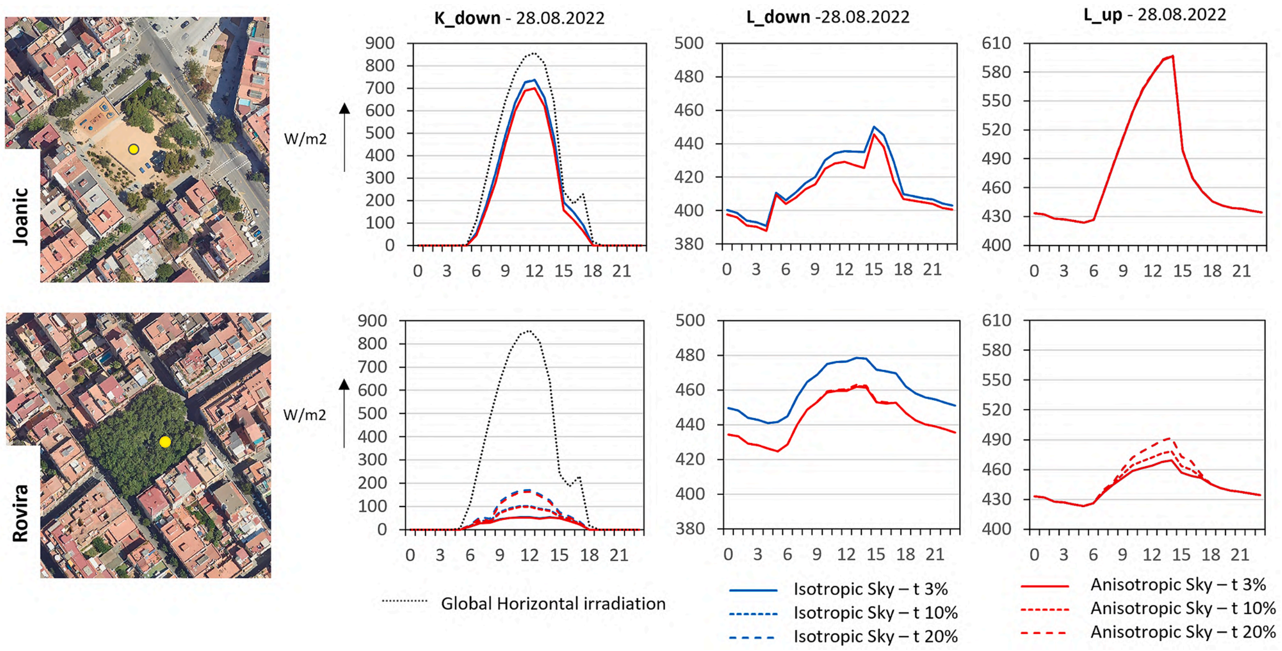

Fig. 7. Hourly trends of incoming shortwave radiation (K_down), incoming longwave radiation (L_down), and outgoing longwave radiation (L_up) on August 28th for various simulation settings at two locations: Joanic, with high sky view factor (SVF) and Rovira, with low SVF due to tree cover. All values are in W/m^2.

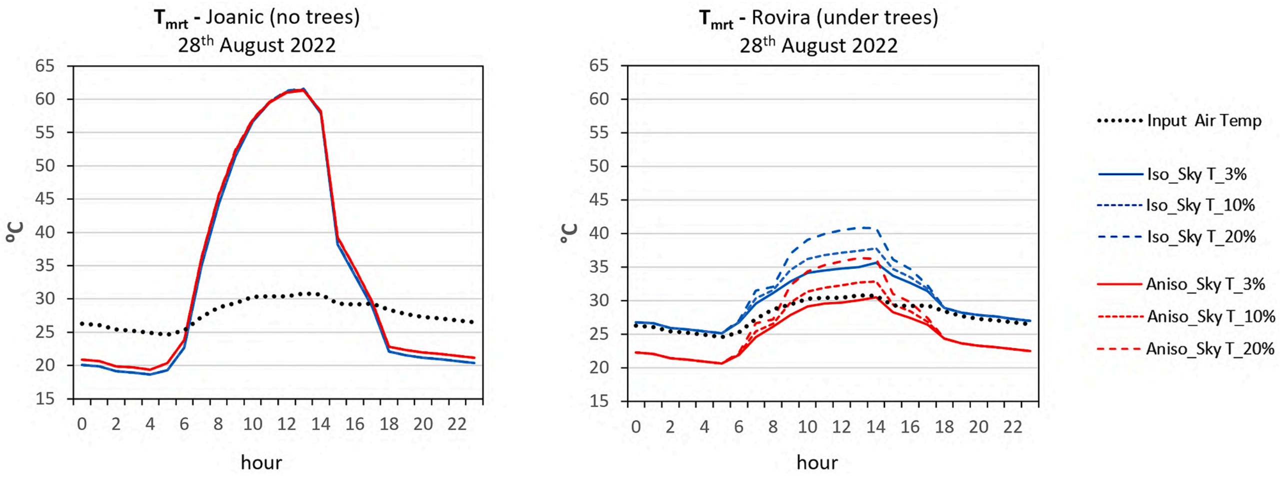

Fig. 8. Hourly T_{mrt} trends on August 28th, comparing different simulation settings at a high-SVF location (Joanic) and a low-SVF location with tree cover (Rovira).

Table 5
Correspondence between PET and T_{mrt} across different levels of physiological stress. The table indicates T_{mrt} thresholds for each stress level, from extreme cold to extreme heat stress.

PET		Physiological Stress	T_{mrt}	
0	4	Extreme cold stress	−20	−13
4	8	Strong cold stress	−13	−6
8	13	Moderate cold stress	−6	2
13	18	Slight cold stress	2	11
18	23	No thermal stress	11	20
23	**29**	**Slight heat stress**	**20**	**30**
29	**35**	**Moderate heat stress**	**30**	**41**
35	**41**	**Strong heat stress**	**41**	**51**
41	**46**	**Extreme heat stress**	**51**	**60**
>	**46**	**Beyond extreme heat stress**	**>**	**60**

The relationship between T_{mrt} and heat stress levels was identified by examining the linear correlation between T_{mrt} and PET. Hourly PET values were modeled using UMEP-SOLWEIG for six representative locations within the study area, selected for their varying SVF, orientations, and tree canopy cover. These include two plazas, namely Joanic (low tree canopy cover) and Rovira (high tree canopy cover), along with four urban canyons: two NE-SW oriented (POI 1 with low tree cover and POI 2 with high tree cover) and two NW-SE oriented (POI 3 with low tree cover and POI 4 with high tree cover). Details of these locations are shown in Figure A.8 of Annex 4.

PET was calculated hourly throughout the 24-hour simulation period. We conducted a regression analysis to measure the relationship between hourly Tmrt and PET, incorporating all observed points and hours. The results, illustrated in Figure A.9 of Annex 4, show a strong linear correlation ($R^2 = 0.97$), indicating a close association between PET levels and the spatial variation in T_{mrt} for the analyzed day.

However, it is important to recognize a significant limitation of this analysis. The spatial variability of air temperature, relative humidity, and wind speed is not accounted for in the PET calculations by UMEP/SOLWEIG. While a recent update to the UMEP tool includes wind

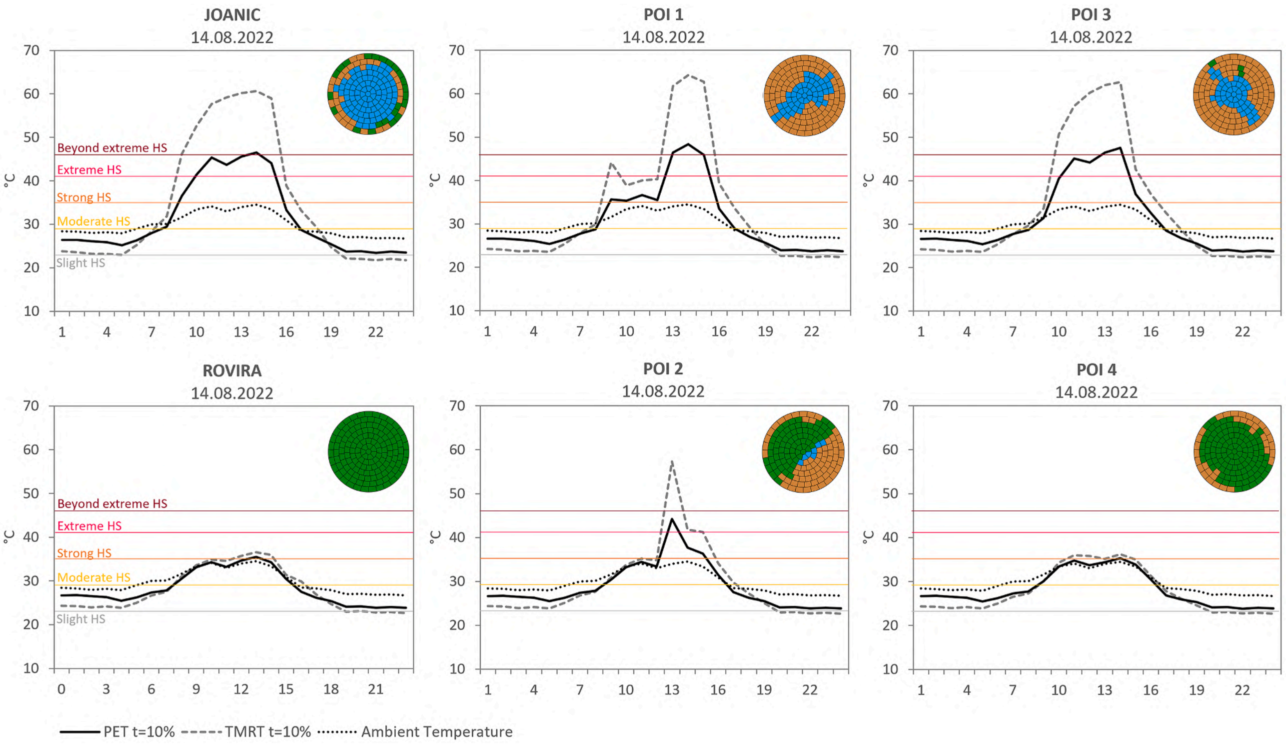

Fig. 9. Hourly variations in T_{mrt} and PET across different urban geometries on August 14, 2022. The six points of interest include four street canyons (POI 1 to 4) and two plazas, i.e., Joanic and Rovira. The graphical representation of sky, trees, and building view factors at each point is reported on the top-left side of each graph.

modeling, T_a and RH remain unmodeled. This study uses an earlier version of UMEP, which does not incorporate the spatial variation of wind speed in PET calculations. Consequently, all variables, except T_{mrt}, are treated as spatially homogeneous across the domain and are set to the hourly values provided by the input meteorological data.

Nevertheless, while addressing this limitation will be a focus of future, more detailed studies, it is essential to emphasize that, under the low wind speed conditions typical of our case study, the correlation between T_{mrt} and PET remains reliable. On August 14th, the wind speeds at 1.5 m ranged from 0.12 to 1.98 m/s. Given these conditions, we can reasonably state that the spatial variation in T_{mrt} predominantly influences OTC variations across the neighborhood.

Table 5 summarizes the T_{mrt} and the corresponding PET values, categorized according to the physiological stress levels outlined by (Matzarakis et al., 1999; Nouri et al., 2022). The T_{mrt} thresholds provided in the table are utilized to identify varying heat stress levels and illustrate its spatial distribution across the district.

We modeled T_{mrt} for the whole district and analyzed histograms of hourly T_{mrt} and corresponding heat stress levels on the hottest day, focusing exclusively on outdoor space between buildings. Based on these results, the critical heat stress period was identified between 09:00 and 20:00 LT, when T_{mrt} values exceeded the threshold of 30 °C in many locations, thus falling into the moderate heat stress category (see Fig. A.10, Annex 4).

4.5. Urban geometry and tree canopy: impacts on heat stress

After modeling T_{mrt} at the district level, we analyzed the influence of tree canopy and urban geometry on heat stress. The six points, as shown in Fig. A.8 (Annex 4), were examined over 24 h on August 14, 2022. Points located in street canyons (POI 1 to 4) have similar SVF but differ in orientation and tree canopy coverage. The two plazas vary significantly in SVF, primarily due to differences in tree canopy density. Diurnal variations in T_{mrt} and PET are illustrated in Fig. 9.

At all points, PET values are consistently lower than T_{mrt}, as PET accounts for convective heat exchange in human thermal balance. However, both T_{mrt} and PET display similar daily trends, supporting the use of T_{mrt} as a reliable proxy for OTC assessments. Notably, areas under tree cover show minimal differences between T_{mrt} and PET. During nighttime, PET can marginally exceed T_{mrt}, due to higher air temperature values than surface temperatures. Conversely, during daytime, T_{mrt} is highly influenced by solar radiation and can reach very high values. In these conditions, the thermal sensation (PET) is generally lower than T_{mrt} due to the beneficial effect of convective heat exchange and lower air temperatures compared to T_{mrt}.

The findings underscore the vital role of trees in reducing T_{mrt} and PET levels throughout the day and in all locations, regardless of openness to the sky and orientation. In Joanic, heat stress is classified as strong to extreme from 9:00 to 16:00, while Rovira remains below the strong heat stress threshold (PET = 35 °C) all day. Maximum PET reaches 48.2 °C in Joanic but only 35.5 °C in Rovira. Similarly, T_{mrt} peaks at 63.9 °C in Joanic compared to just 36.6 °C in Rovira, with Revolució showing a comparable trend (PET of 46.5 °C and T_{mrt} of 60.7 °C).

In the NW-SE urban canyon with trees (POI 4), heat stress remains moderate (maximum PET is 35.3 °C). In contrast, in the same orientation without trees (POI 3), it escalates to strong, extreme, and beyond extreme levels by 14:00, reaching a PET of 47.6 °C. In the NE-SW canyon without trees (POI 1), building shadows reduce heat stress in the morning between 9:00 and 11:00, but it peaks at 48.4 °C by 14:00, the highest of all points, with extreme heat stress from 13:00 to 15:00.

These results highlight the dynamic effect of urban geometry on the street-level thermal environment depending on time and orientation. In this case, a narrow canyon geometry significantly reduces heat stress in the morning, but has a negligible impact in the afternoon. However, trees in the same orientation (POI 2) lower the maximum PET to 44.2 °C, underscoring their effectiveness in mitigating heat stress during peak solar hours, in narrow street canyons, too. Given that these results are from August 14th, trees would likely have an even greater effect closer to the summer solstice when solar elevation is highest.

Using district-scale hourly T_{mrt}, we generated pixel-based spatial

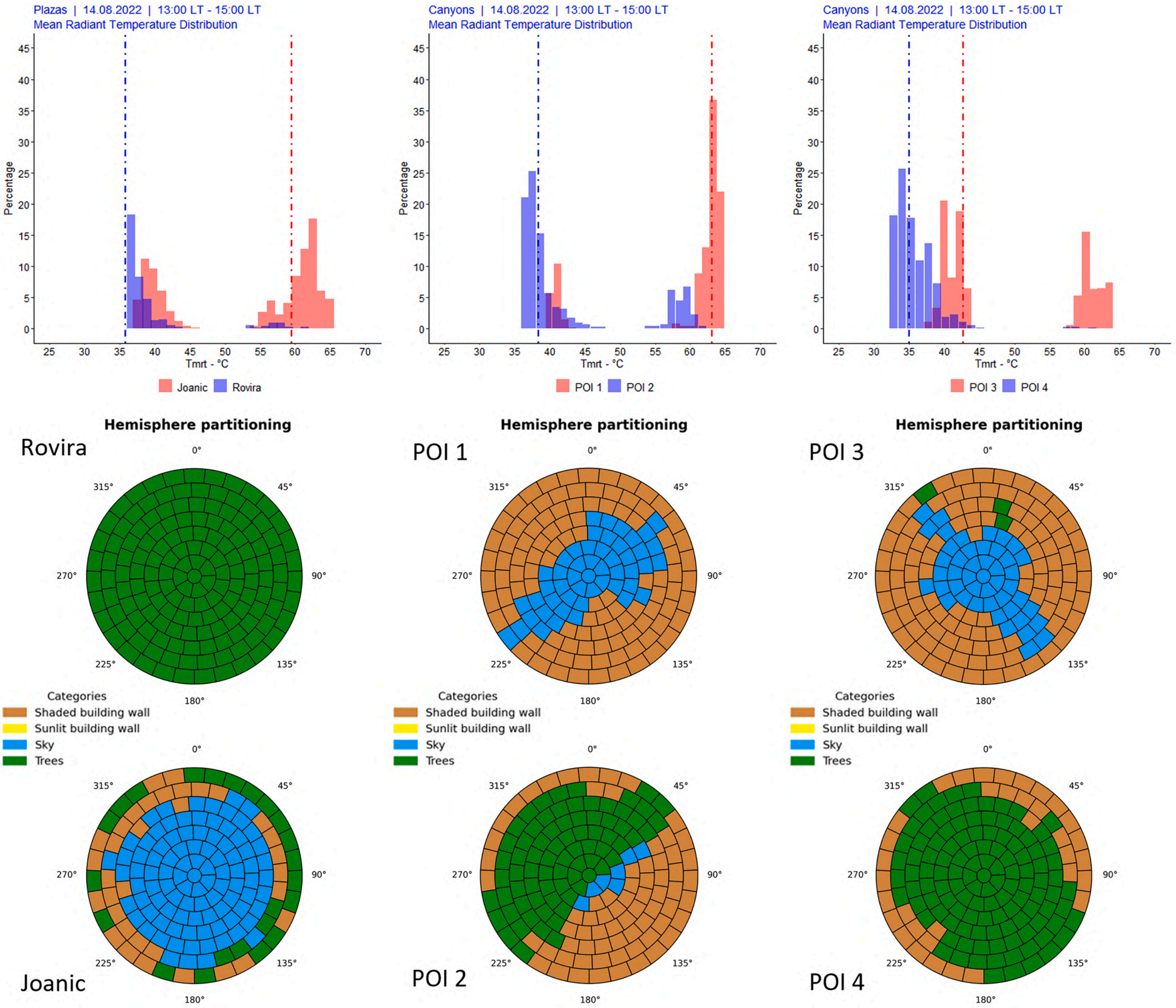

Fig. 10. Histograms showing the distribution of T_{mrt} values in Joanic and Rovira plazas, as well as in the four urban canyons (POIs 1 to 4), for the peak heat hours interval, between 13:00 and 15:00. The dotted lines indicate the median T_{mrt}. The bottom of the figure includes a graphical representation of the sky, trees, and building's view factors.

average maps of T_{mrt} by calculating the mean T_{mrt} for each pixel over three-hour intervals: 10:00–12:00, 13:00–15:00, and 16:00–18:00. This involved averaging multiple rasters for each time period, resulting in a spatially resolved representation of heat stress across the district for each three-hour stack (refer to Fig. A.11 in Annex 5).

The resulting maps show the time-dependent effect that urban geometry and orientation have on the street-level thermal environment. In the morning, the NW-SE canyons experience worse conditions than the NE-SW ones despite similar SVF values. More specifically, the NW-SE canyons experience strong to extreme levels of heat stress, whereas the NE-SW canyons remain within the moderate threshold. The situation is reversed in the afternoon: the NW-SE canyons experience moderate heat stress, while the NE-SW canyons experience strong and extreme levels. During the hottest hours of the day, from 13:00 to 15:00, the effect of urban geometry is negligible due to the high solar elevation, with both orientations showing extreme and beyond-extreme heat stress levels.

However, on streets with trees, T_{mrt} remains within moderate levels. During peak heat hours, the effects of tree canopy and urban orientation become even more pronounced when analyzing the entire canyon and plazas (Fig. 10).

The tree canopy significantly reduces heat stress in the plazas during the early afternoon. Median T_{mrt} values (dash-dot lines in the histograms) highlight the cooling effect of trees, dropping from 60 °C in Joanic (and similar values in Revolució) to 35 °C in Rovira Plaza.

When comparing similarly oriented canyons with different tree canopy coverage (POI 1 vs. POI 2 and POI 3 vs. POI 4), trees are shown to substantially lower peak T_{mrt} values between 13:00 and 16:00. The reduction in median T_{mrt} ranges from −22 °C in the NE-SW oriented canyon (POI 2) to −6 °C in the NW-SE oriented canyon (POI 4).

Orientation also plays a significant role when comparing the NE-SW canyon (POI 1) with the NW-SE canyon (POI 3). At peak heat hours, the NE-SW canyon shows a much higher median T_{mrt} of around 63 °C compared to the NW-SE canyon's 43 °C, a difference of about −20 °C. Notably, the NW-SE canyon (POI 3) shows lower T_{mrt} than Joanic Plaza, which reaches 60 °C, caused by a high SVF. Similarly, POI 2 (NE-SW orientation) experiences greater heat than POI 4 (NW-SE orientation), with median T_{mrt} of 38 °C and 35 °C, respectively. This underscores the combined impact of vegetation and urban geometry on microclimate regulation.

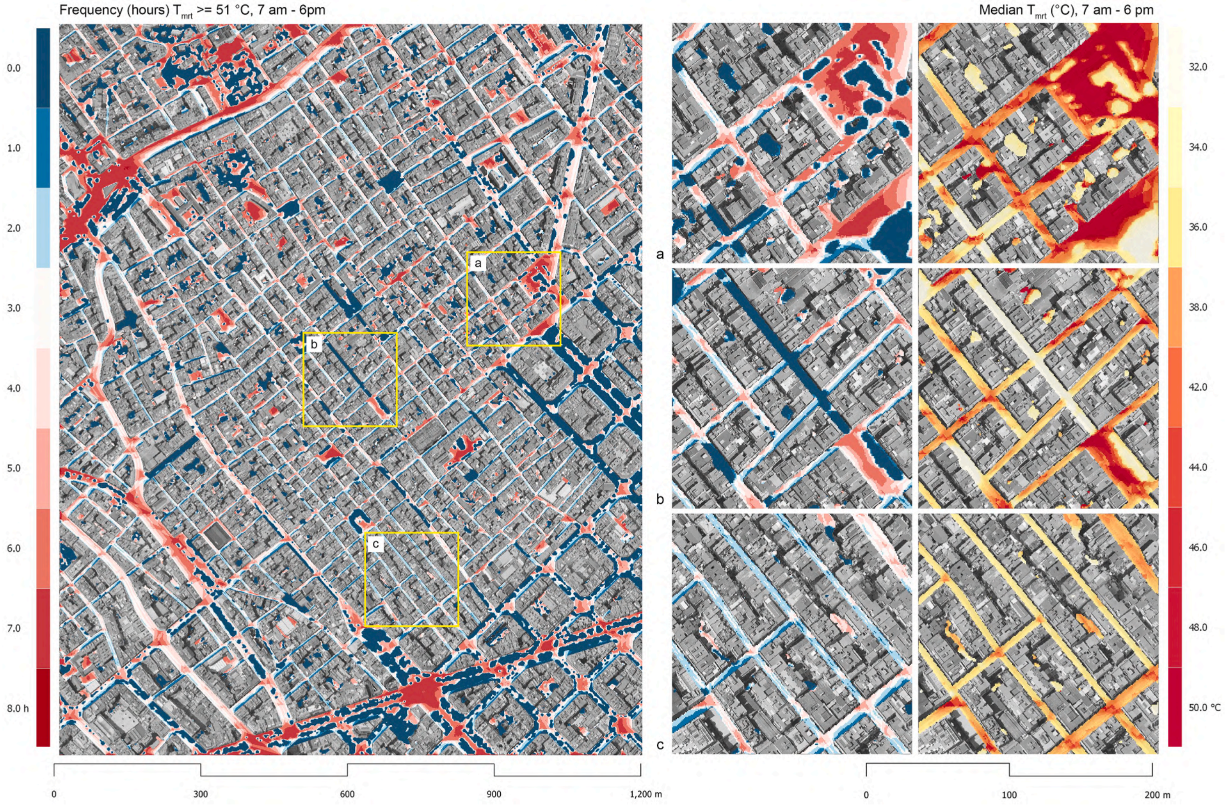

Fig. 11. Cumulative heat stress map for August 14th, 2022, based on T_{mrt} modeling. The blue-to-red color scale indicates T_{mrt} exceeding 51 °C. Zoomed-in sections (a, b, and c) provide detailed views and median T_{mrt} values from 09:00 to 20:00 LT.

Ultimately, while tree canopy consistently alleviates heat stress throughout the day, canyon orientation plays a role in reducing heat stress at specific times. Combining both strategies enhances heat mitigation, and understanding orientation benefits can guide more effective climate-proof design.

4.6. District-scale heat-scapes: mapping cumulative heat stress

Cumulative Heat Stress, as defined in this study, captures the duration and intensity of heat exposure over an entire day. By mapping hourly T_{mrt} variations and aggregating hazard levels, this approach reflects the prolonged impact of urban microclimates, helping urban planners identify persistent heat-prone areas for targeted interventions.

Using T_{mrt} simulations for August 14th, 2022, we developed a replicable district-scale cumulative heat stress map based on 24-hour modeling with an anisotropic sky model and 10 % tree canopy solar transmissivity. The map captures microscale spatial patterns of heat stress between 09:00 and 20:00 LT, highlighting the number of hours T_{mrt} exceeds the 51 °C extreme heat stress threshold (PET-based; see Table 5). Fig. 11 displays the map with a blue-to-red color scale, where dark red indicates the most affected areas, and includes zoomed-in sections (a, b, c) with corresponding pixel-based median T_{mrt} values.

The map clearly outlines cool- and hot-spot areas across the Gracia district, aiding in identifying hazardous outdoor spaces. In the most extreme cases (dark red areas), heat stress levels exceeded 51 °C for up to 8 h during the day, while in the least affected areas (dark blue), temperatures remained below this threshold. The map reveals that 'cool' spots are predominantly located under tree canopies, whether in plazas or urban canyons, with zero hours exceeding the extreme threshold. The dense street network in Gracia, featuring narrow canyons that provide significant shading, also helps reduce heat stress duration to approximately 3 to 4 h, compared to open spaces or streets with high SVF and minimal vegetation, which endure up to 7 or 8 h of extreme heat stress.

In Fig. 11, zoom-in (a) highlights outdoor spaces with prolonged extreme heat exposure, shown in dark red, due to limited shading and high SVF. Zoom-in (b) depicts areas with more varied heat stress levels, likely reflecting the presence of tree cover and improved shading. Zoom-in (c) shows generally moderate heat stress, where narrow street canyons provide partial shading, though less effectively than tree canopies.

The spatial distribution of heat stress in Gracia is highly uneven. Overlaying heat frequency data onto the urban fabric reveals a distinct 'heat-scape,' identifying zones more vulnerable to extreme temperatures. This analysis underscores how urban geometry, orientation, and vegetation shape local heat patterns, reinforcing the role of design in mitigating heat stress.

The cumulative heat stress map developed in this study offers a replicable and operational tool for assessing and addressing urban heat risks, providing actionable insights for climate-resilient design. Unlike previous studies (Aghamolaei et al., 2020; Nazarian et al., 2019), which often rely on small-scale idealized simulations or overlook the role of tree canopies in outdoor thermal comfort, this approach captures the fine-grained spatial variability of heat stress across a real urban district.

5. Discussion

5.1. Heat stress map as a tool for climate-responsive planning and design

This study demonstrates the value of high-resolution microclimate simulations for capturing the complex climate dynamics of urban environments. The findings emphasize the need for district-scale analysis to inform climate-responsive planning, moving beyond the localized focus of single-canyon studies. By mapping cumulative heat stress across an entire neighborhood, the results reveal how vegetation, urban form, open spaces, and grid orientation shape thermal conditions. This highlights the necessity for context-specific strategies that respond to neighborhood-scale microclimate variability, advancing from generic guidelines toward targeted, climate-resilient urban design.

The SOLWEIG model proved effective for analyzing the spatial and temporal variability of T_{mrt} across an entire district, with a resolution sufficient to inform climate-adaptive urban design. The resulting cumulative heat stress map offers a foundation for evidence-based planning and regulatory frameworks, emphasizing urban geometry and the strategic placement of green infrastructure. Urban trees, in particular, emerged as critical assets for mitigating peak radiant temperatures, even in narrow streets, reinforcing their essential role in building heat-resilient cities.

Prior research (Chang & Li, 2014; A. Chen et al., 2014; de Quadros & Mizgier, 2023; Lee et al., 2020) reinforces the role of urban trees in mitigating heat stress through shading and evapotranspiration. These studies also emphasize that the effectiveness of cooling depends on canopy density, species selection, and spatial arrangement—critical considerations for designing impactful urban greening strategies.

While some studies (Correa et al., 2012; Gao et al., 2024) have raised concerns about trees potentially reducing convective cooling and contributing to nighttime warming, our findings show that their daytime cooling benefits far outweigh these effects. Also, trees provide substantially greater cooling than grass or other permeable surfaces.

During the hottest hours, a comparison between Joanic and Revolució showed that the different paving materials had little effect on the measured T_g despite their noticeable impact on ground surface temperature. Conversely, the effect of trees is evident in Rovira, with T_g 12,8 °C lower than Joanic and 11,6 °C lower than Revolució.

The results also emphasize the need to consider the temporal variability of shade provision as a strategy to reduce heat stress. The spatial distribution of T_{mrt} and heat stress changes markedly throughout the day. In compact urban environments like Gràcia, urban geometry can effectively mitigate pedestrian heat stress during the morning (until 12:00 LT) and again in the late afternoon (after 16:00 LT). On the other hand, in the time window from 13:00 to 15:00, urban geometry has a negligible impact due to high solar elevations. At the same time, tree shade significantly reduces heat stress from beyond extreme to moderate levels, highlighting the importance of strategic tree planting during this critical timeframe.

5.2. The SOLWEIG model: insights from urban microclimate simulations

The study first aims to optimize microclimate simulations using the UMEP-SOLWEIG model, guided by an on-site campaign. However, the findings are specific to Mediterranean climates, with the Gracia district of Barcelona— a compact urban neighborhood— serving as the test area. It is important to note that the comparison results should not be considered as validation of the SOLWEIG model. A larger dataset and extended measurement period, along with improved T_{mrt} measurement methods (e.g., radiometers), would be necessary, as the T_g-based calculation is less accurate in outdoor, sunny conditions (Banfi et al., 2022; Johansson et al., 2014). Nevertheless, comparing measured and simulated data helped shed light on the factors influencing outdoor thermal comfort and refine key parameters.

The deviations between SOLWEIG simulations and measurement-based T_{mrt} differ for sunny and shaded locations. For sunny areas, the primary cause of deviation is the uncertainty in input radiation data, sourced from an urban weather station located 2.5 km from Gracia. The data, averaged over 30-minute intervals, may not match the actual solar irradiation during the measurement period, potentially leading to T_{mrt} overestimation. However, the overestimation (ranging from +6.6 °C to +8.7 °C for Joanic and Rovira) falls within the accepted T_{mrt} error range of ±5 °C, which corresponds to a perceived thermal sensation range of ±2 °C (Banfi et al., 2022). These differences are consistent with those found in other SOLWEIG validation studies (Briegel et al., 2023).

In shaded areas, the SOLWEIG model is highly sensitive to variations in tree solar transmissivity and the sky model. The anisotropic sky model, which accounts for changes in diffuse shortwave and longwave radiation based on zenith angle, proves more accurate. It notably reduces incoming shortwave radiation by up to 45 W/m^2 at noon compared to the isotropic model and slightly decreases longwave radiation by 1–4 %, depending on tree canopy transmissivity. While the anisotropic model has minimal effect on areas with direct solar exposure (<0.5 °C), it lowers T_{mrt} by 4.5 to 5 °C in shaded areas, both during the day and at night, which is consistent with the 3 °C reduction observed in Gothenburg (Wallenberg et al., 2023).

In shaded areas, tree solar transmissivity significantly influences T_{mrt} estimation, with variations up to ±5 °C. For our case studies, the best alignment with real-world data was achieved using the anisotropic sky model and a tree solar transmissivity of 10 %. Given the model's sensitivity to these parameters, adjustments based on local conditions and observational data are essential for accurate T_{mrt} simulations. Additionally, simulation duration impacts T_{mrt} estimates, as shorter periods may not capture full shadow effects and surface temperature variations (Lindberg et al., 2008). To improve accuracy, a buffer period of at least three hours before and after the target time is recommended.

5.3. Limitations for large-scale application

Upscaling high-resolution urban microclimate models involves navigating complex computational challenges. In SOLWEIG the simulation process starts with calculating the SVF, which is crucial for accurate T_{mrt} modeling. Using the UMEP tool, we optimized this by selecting a method with 153 shadow images, which proved more efficient than the traditional 655-image approach. However, computational demand increases exponentially with larger spatial extents or higher resolution.

To evaluate computational efficiency, we analyzed SVF calculations for square areas with side lengths of 250 m, 500 m, 1000 m, 2000 m, and 4000 m. We also examined the impact of different resolutions, testing pixel sizes ranging from 1 m to 3 m for the largest area (4000 m). This evaluation highlights the trade-offs between computational efficiency and resolution accuracy.[1] Simulation times vary notably for the 4000 m square area: from 31.44 h at a 1 m resolution to just 1.02 h at a 3 m resolution.

Similarly, T_{mrt} simulations, which account for both isotropic and anisotropic sky conditions, show that while anisotropic simulations are more efficient in outcomes, they are computationally intensive. For the 4000 m extent, T_{mrt} simulation times range from 10.21 h at a 1 m resolution to 0.87 h at a 3 m resolution. While the T_{mrt} computation may require less time, it is essential to consider that the SVF is a prerequisite for T_{mrt} simulations. Fig. 12 highlights how spatial resolution and extent dramatically affect computation time.

According to our results, a 1-meter spatial resolution simulation of SVF and T_{mrt} for the whole city of Barcelona (approximately 101.4 km^2) would take an estimated 374.14 h (15.59 days) for SVF and 94.85 h (3.95 days) for T_{mrt}. This underscores the substantial computational effort and resource intensity required for city-wide urban microclimate simulations.

Currently, UMEP stands out as one of the most effective tools for scaling up district-wide microclimate modeling, offering a distinct advantage over other schemes focused on building-scale outdoor simulations. However, while promising approaches are explored, such as the use of graphics processing unit (GPU) parallel computing to accelerate simulations time (Li & Wang, 2021), it remains crucial to address these challenges and continue refining methodologies to enhance efficiency and feasibility for large-scale city simulations.

---

[1] The simulations were conducted on a machine equipped with a 12th Gen Intel(R) Core (TM) i9-12900H processor, operating at 2500 MHz with 14 cores and 20 logical processors. The machine also boasts 64 GB of RAM and a GPU with Intel(R) Iris (R) Xe Graphics 31.8 GB.

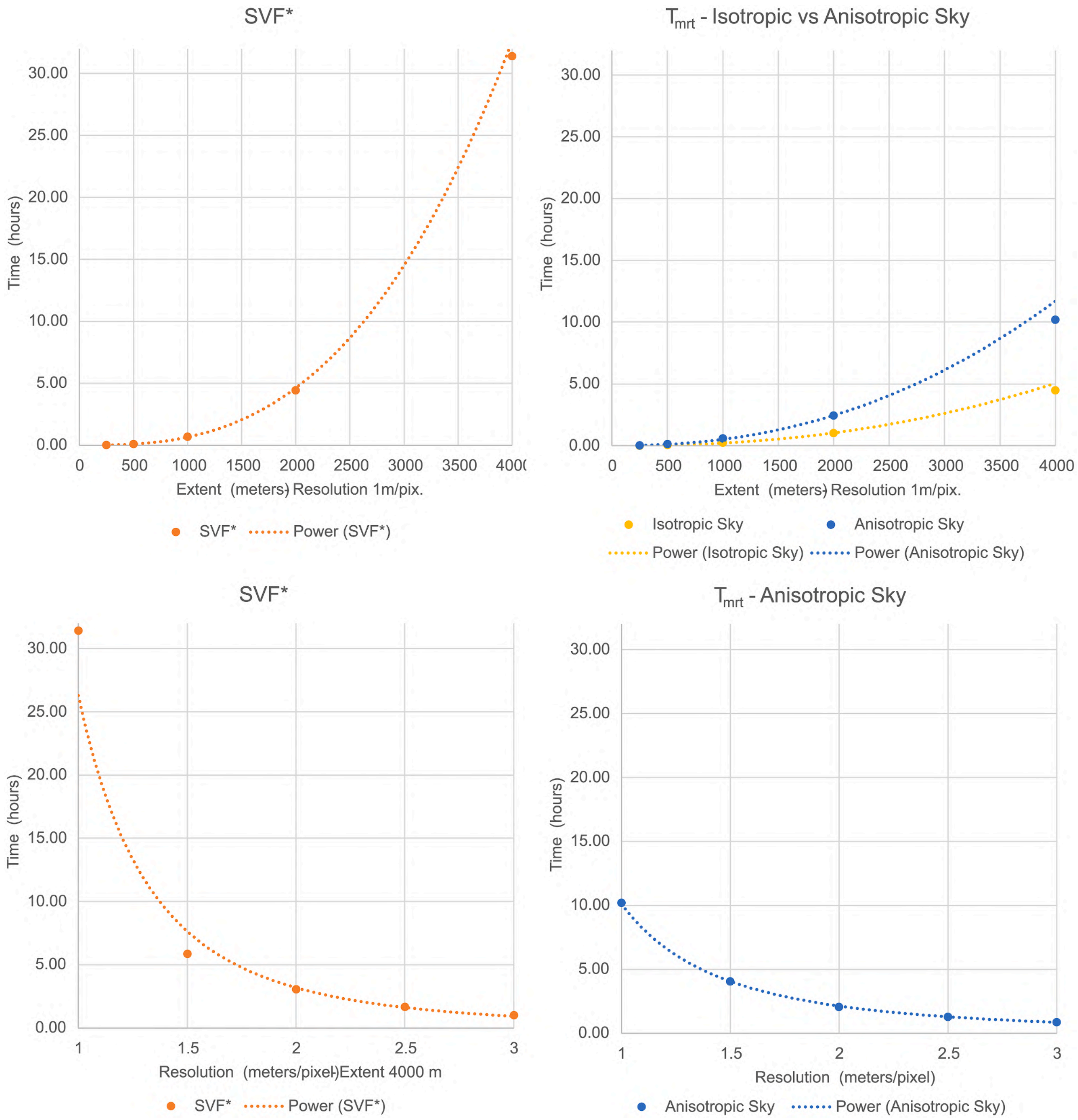

Fig. 12. Impact of different spatial resolutions and extents on simulation time for SVF (*Method with 153 shadow images instead of 655), and T_{mrt}. The top two images demonstrate the rise in simulation times as the study area grows from 250 m to 4000 m. The bottom two images highlight the impact of decreasing spatial resolution for a fixed area of 4000 m per side.

5.4. *Study constraints and future directions*

While this research offers valuable insights into the microclimatic effects of urban form and tree canopy, some limitations need to be acknowledged. First, the simulations rely on specific meteorological data from a representative weather station, which may not fully capture localized weather variations across the entire district. The lack of spatially heterogeneous data for air temperature, wind speed, and relative humidity limits the precision of PET estimations. For instance, the measured air temperature was about 32,1 °C in Joanic, 30 °C in Rovira and 33,1 °C in Revolució.

Future research should focus on integrating wind, air temperature, and humidity models into T_{mrt} and PET simulations. This would allow for more nuanced thermal comfort assessments that capture the full range of environmental variables influencing heat stress. Expanding the geographic scope of the simulations to cover larger urban areas or entire cities would also provide more comprehensive insights into the distribution of heat stress across different urban fabrics.

Additionally, the use of spatially homogeneous vegetation data may not accurately reflect variations in tree canopy density and solar transmissivity. Future studies could incorporate more detailed vegetation models to account for differences in canopy structure. Similarly, using constant albedo and emissivity values for building façades may oversimplify the thermal dynamics of urban surfaces.

Another limitation is the short-term nature of the campaign, which focused on only two days, three specific locations, and limited hours.

While these conditions were selected to target key microclimatic scenarios, the restricted timeframe and scope limit the ability to capture the full range of variations in the study area. Expanding both the number of measurement points and the duration of the campaign would improve the accuracy of microclimate model simulations and provide more comprehensive validation.

Finally, as computational tools evolve, future studies could explore using advanced machine learning algorithms to enhance the efficiency of VHR microclimate simulations, reducing computation time while maintaining accuracy.

6. Conclusions

This study underscores the critical role of microclimate modeling in mitigating urban heat stress amid global warming, focusing on the development of a methodology for cumulative heat stress maps using high-resolution district-scale simulations in a Mediterranean climate. By mapping the spatiotemporal distribution of heat stress, we offer a replicable approach for identifying heat-prone areas and informing climate-responsive interventions.

The findings demonstrate that urban geometry, street network orientation, and tree canopy cover play pivotal roles in shaping both the intensity and duration of cumulative heat stress. Areas with high SVF and minimal vegetation experience prolonged periods of extreme heat stress, often exceeding thresholds of 51 °C for several hours. In contrast, tree canopies can lower T_{mrt} by >20 °C during peak heat hours. The study also highlights that NW-SE oriented urban canyons are less exposed to heat stress compared to NE-SW orientations, especially when tree cover is present, underscoring the importance of urban morphology and urban green in outdoor thermal comfort. Heat stress frequency maps further show that plazas with dense tree cover maintain moderate thermal stress, whereas open spaces without shade are subjected to extreme conditions.

Plazas and street grids are crucial elements in urban neighborhoods, directly influencing thermal comfort and the well-being of residents. The study illustrates that these spaces, particularly in Gracia, are key determinants of thermal conditions, and their characteristics can be improved with the addition of urban vegetation, especially trees.

Integrating cumulative heat stress maps into urban planning and design can guide the development of climate-sensitive strategies, enhancing outdoor thermal comfort and reducing heat exposure in public spaces. Our method provides a practical tool for evaluating heat mitigation strategies at the district level, supporting data-driven decision-making for urban resilience guiding urban regulations and climate-proof plans.

For example, the findings can be relevant to Barcelona's Climate Shelter Program, which aims to transform public spaces into climate-resilient areas with increased vegetation and shading. By offering detailed insights into the spatial and temporal distribution of heat stress, the study enables policymakers to prioritize interventions where they are most needed, ensuring effective cooling solutions for vulnerable populations. Specific areas, such as schoolyards, playgrounds, and public squares, can be targeted for tailored climate-responsive measures, with schools benefiting from morning shading and leisure spaces requiring enhanced afternoon cooling strategies.

CRediT authorship contribution statement

Nicola Colaninno: Writing – review & editing, Writing – original draft, Visualization, Validation, Supervision, Project administration, Methodology, Investigation, Formal analysis, Data curation, Conceptualization. **Agnese Salvati:** Writing – review & editing, Writing – original draft, Visualization, Validation, Supervision, Project administration, Methodology, Investigation, Formal analysis, Data curation, Conceptualization. **Judit Lopez-Besora:** Writing – review & editing, Visualization, Methodology, Investigation. **Michele Morganti:** Writing – review & editing, Writing – original draft, Validation, Supervision, Methodology, Investigation, Conceptualization.

Declaration of competing interest

The authors declare the following financial interests/personal relationships which may be considered as potential competing interests:

Nicola Colaninno reports administrative support, article publishing charges, and equipment, drugs, or supplies were provided by Polytechnic University of Milan. Agnese Salvati reports equipment, drugs, or supplies was provided by Polytechnic University of Catalonia. If there are other authors, they declare that they have no known competing financial interests or personal relationships that could have appeared to influence the work reported in this paper.

Acknowledgements

This research was supported by the project 'MultiCAST - Multiscale Thermal-related Urban Climate Analysis and Simulation Tool,' which has received funding from the European Union's Horizon 2020 research and innovation programme under the Marie Sklodowska-Curie grant agreement No 101028035. The research was also supported by the project PID2020-116036RB-I00, funded by MICIU/AEI/10.13039/501100011033.

Supplementary materials

Supplementary material associated with this article can be found, in the online version, at doi:10.1016/j.scs.2025.106498.

Data availability

Data will be made available on request.

References

Aghamolaei, R., Azizi, M. M., Aminzadeh, B., & Mirzaei, P. A. (2020). A tempo-spatial modelling framework to assess outdoor thermal comfort of complex urban neighbourhoods. *Urban Climate, 33*, Article 100665. https://doi.org/10.1016/J.UCLIM.2020.100665

Ajuntament de Barcelona. (2023). *Arbrat viari de la ciutat de Barcelona - Conjunts de dades - Open data Barcelona*. https://opendata-ajuntament.barcelona.cat/data/ca/dataset/arbrat-viari.

Alchapar, N. L., Correa, E. N., & Cantón, M. A. (2014). Classification of building materials used in the urban envelopes according to their capacity for mitigation of the urban heat island in semiarid zones. *Energy and Buildings, 69*, 22–32. https://doi.org/10.1016/J.ENBUILD.2013.10.012

Aleksandrowicz, O., Zur, S., Lebendiger, Y., & Lerman, Y. (2020). Shade maps for prioritizing municipal microclimatic action in hot climates: Learning from Tel Aviv-Yafo. *Sustainable Cities and Society, 53*. https://doi.org/10.1016/J.SCS.2019.101931

ASHRAE. (2001). *ASHRAE fundamentals handbook 2001*. American Society of Heating, Refrigerating and Air-Conditioning Engineers - ASHRAE.

Bäcklin, O., Lindberg, F., Thorsson, S., Rayner, D., & Wallenberg, N. (2021). Outdoor heat stress at preschools during an extreme summer in Gothenburg, Sweden - preschool teachers' experiences contextualized by radiation modelling. *Sustainable Cities and Society*, 75. https://doi.org/10.1016/J.SCS.2021.103324

Banfi, A., Tatti, A., Ferrando, M., Fustinoni, D., Zanghirella, F., & Causone, F. (2022). An experimental technique based on globe thermometers for the measurement of mean radiant temperature in urban settings. *Building and Environment, 222*, Article 109373. https://doi.org/10.1016/J.BUILDENV.2022.109373

Barišić, I., Grubeša, I. N., Krstić, H., & Kubica, D. (2022). Field and laboratory assessment of different concrete paving materials thermal behavior. *Sustainability, 14*(11), 6638. https://doi.org/10.3390/SU14116638. *2022, Vol. 14, Page 6638*.

Bobb, J. F., Peng, R. D., Bell, M. L., & Dominici, F. (2014). Heat-related mortality and adaptation to heat in the United States. *Environmental Health Perspectives, 122*(8), 811–816. https://doi.org/10.1289/ehp.1307392

Boland, J., Ridley, B., & Brown, B. (2008). Models of diffuse solar radiation. *Renewable Energy, 33*(4), 575–584. https://doi.org/10.1016/J.RENENE.2007.04.012

Briegel, F., Makansi, O., Brox, T., Matzarakis, A., & Christen, A. (2023). Modelling long-term thermal comfort conditions in urban environments using a deep convolutional encoder-decoder as a computational shortcut. *Urban Climate*, 47. https://doi.org/10.1016/J.UCLIM.2022.101359

Bruse, M., & Fleer, H. (1998). Simulating surface-plant-air interactions inside urban environments with a three dimensional numerical model. *Environmental Modelling and Software, 13*(3–4), 373–384. https://doi.org/10.1016/S1364-8152(98)00042-5

Cantón, M. A., Cortegoso, J. L., & de Rosa, C. (1994). Solar permeability of urban trees in cities of western Argentina. *Energy and Buildings, 20*(3), 219–230. https://doi.org/10.1016/0378-7788(94)90025-6

Chakraborty, T., Hsu, A., Manya, D., & Sheriff, G. (2019). Disproportionately higher exposure to urban heat in lower-income neighborhoods: A multi-city perspective. *Environmental Research Letters, 14*(10), Article 105003.

Chang, C. R., & Li, M. H. (2014). Effects of urban parks on the local urban thermal environment. *Urban Forestry & Urban Greening, 13*(4), 672–681. https://doi.org/10.1016/J.UFUG.2014.08.001

Chen, A., Yao, X. A., Sun, R., & Chen, L. (2014). Effect of urban green patterns on surface urban cool islands and its seasonal variations. *Urban Forestry & Urban Greening, 13*(4), 646–654. https://doi.org/10.1016/J.UFUG.2014.07.006

Chen, L., Ng, E., An, X., Ren, C., Lee, M., Wang, U., & He, Z. (2012). Sky view factor analysis of street canyons and its implications for daytime intra-urban air temperature differentials in high-rise, high-density urban areas of Hong Kong: A GIS-based simulation approach. *International Journal of Climatology, 32*(1), 121–136. https://doi.org/10.1002/joc.2243

Correa, E., Ruiz, M. A., Canton, A., & Lesino, G. (2012). Thermal comfort in forested urban canyons of low building density. An assessment for the city of Mendoza, Argentina. *Building and Environment, 58*, 219–230. https://doi.org/10.1016/J.BUILDENV.2012.06.007

de Quadros, B. M., & Mizgier, M. G. O. (2023). Urban green infrastructures to improve pedestrian thermal comfort: A systematic review. *Urban Forestry & Urban Greening*, Article 128091.

Dear, R.de (1988). Ping-pong globe thermometers for mean radiant temperatures. *H and V Engineer, 60*(681), 10–11. https://researchers.mq.edu.au/en/publications/ping-pong-globe-thermometers-for-mean-radiant-temperatures.

Ding, X., Zhao, Y., Strebel, D., Fan, Y., Ge, J., & Carmeliet, J. (2024). A WRF-UCM-SOLWEIG framework for mapping thermal comfort and quantifying urban climate drivers: Advancing spatial and temporal resolutions at city scale. *Sustainable Cities and Society, 112*, Article 105628. https://doi.org/10.1016/J.SCS.2024.105628

Ding, X., Zhao, Y., Strebel, D., Fan, Y., Ge, J., & Carmeliet, J. (2025). A cross-scale methodological framework for the quantification of the impact of urban features on intra-city microclimate. *EGU General Assembly 2024*. https://doi.org/10.5194/EGUSPHERE-EGU24-14606

Dirksen, M., Ronda, R. J., Theeuwes, N. E., & Pagani, G. A. (2019). Sky view factor calculations and its application in urban heat island studies. *Urban Climate*, 30. https://doi.org/10.1016/j.uclim.2019.100498

Diz-Mellado, E., Rubino, S., Fernández-García, S., Gómez-Mármol, M., Rivera-Gómez, C., & Galán-Marín, C. (2021). Applied machine learning algorithms for courtyards thermal patterns accurate prediction. *Mathematics, 9*(10), 1142. https://doi.org/10.3390/MATH9101142. *2021, Vol. 9, Page 1142*.

Elmarakby, E., & Elkadi, H. (2024). Prioritising urban heat island mitigation interventions: Mapping a heat risk index. *Science of The Total Environment, 948*, Article 174927. https://doi.org/10.1016/J.SCITOTENV.2024.174927

Emmanuel, R., & Fernando, H. J. S. (2007). Urban heat islands in humid and arid climates: Role of urban form and thermal properties in Colombo, Sri Lanka and Phoenix, USA. *Climate Research, 34*(3), 241–251. https://doi.org/10.3354/cr00694

Erell, E., Pearlmutter, D., Boneh, D., & Kutiel, P. B. (2014). Effect of high-albedo materials on pedestrian heat stress in urban street canyons. *Urban Climate, 10*(P2), 367–386. https://doi.org/10.1016/j.uclim.2013.10.005

Erell, E., Pearlmutter, D., & Williamson, T. (2012). Urban microclimate : Designing the spaces between buildings. *Urban Microclimate*. https://doi.org/10.4324/9781849775397

Evola, G., Costanzo, V., Magrì, C., Margani, G., Marletta, L., & Naboni, E. (2020). A novel comprehensive workflow for modelling outdoor thermal comfort and energy demand in urban canyons: Results and critical issues. *Energy and Buildings, 216*, Article 109946. https://doi.org/10.1016/J.ENBUILD.2020.109946

Evola, G., Costanzo, V., Marletta, L., Nocera, F., Detommaso, M., & Urso, A. (2021). An investigation on the radiant heat balance for different urban tissues in Mediterranean climate: A case study. *Journal of Physics: Conference Series, 2042*(1). https://doi.org/10.1088/1742-6596/2042/1/012046

Gál, C. V., & Kántor, N. (2020). Modeling mean radiant temperature in outdoor spaces, A comparative numerical simulation and validation study. *Urban Climate, 32*, Article 100571. https://doi.org/10.1016/J.UCLIM.2019.100571

Gao, K., Feng, J., & Santamouris, M. (2024). Are grand tree planting initiatives meeting expectations in mitigating urban overheating during heat waves? *Sustainable Cities and Society*, 113. https://doi.org/10.1016/j.scs.2024.105671

Georgi, J. N., & Dimitriou, D. (2010). The contribution of urban green spaces to the improvement of environment in cities: Case study of Chania, Greece. *Building and Environment, 45*(6), 1401–1414. https://doi.org/10.1016/J.BUILDENV.2009.12.003

Glazer, J. L. (2005). Management of heatstroke and heat exhaustion. *American Family Physician, 71*(11), 2133–2140. https://www.aafp.org/pubs/afp/issues/2005/0601/p2133.html.

Björn, H., Fredrik, L., David, R., & Sofia, T. (2015). How to transform the standing man from a box to a cylinder – a modified methodology to calculate mean radiant temperature in field studies and models. In *ICUC9 - 9th international conference on urban climate jointly with 12th symposium on the urban environment*.

Höppe, P. (1992). Ein neues verfahren zur bestimmung der mittleren strahlungstemperatur im Freien. *Wetter Und Leben, 44*(1–3), 147–151.

Huang, J., Tang, X., Jones, P., Hao, T., Tundokova, R., Walmsley, C., Lannon, S., Frost, P., & Jackson, J. (2024). Mapping pedestrian heat stress in current and future heatwaves in Cardiff, Newport, and Wrexham in Wales, UK. *Building and Environment, 251*, Article 111168. https://doi.org/10.1016/J.BUILDENV.2024.111168

Inostroza, L., Palme, M., & De La Barrera, F. (2016). A heat vulnerability index: Spatial patterns of exposure, sensitivity and adaptive capacity for Santiago de Chile. *Plos One, 11*(9), Article e0162464. https://doi.org/10.1371/JOURNAL.PONE.0162464

Institut Cartogràfic i Geològic de Catalunya. (n.d.). *LiDAR Territorial | icgc*. Retrieved April 25, 2025, from https://www.icgc.cat/ca/Geoinformacio-i-mapes/Dades-i-productes/Bessons-digitals-Elevacions/LiDAR-Territorial.

Jandaghian, Z., & Akbari, H. (2018). The effects of increasing surface reflectivity on heat-related mortality in Greater Montreal Area, Canada. *Urban Climate, 25*, 135–151. https://doi.org/10.1016/j.uclim.2018.06.002

Jänicke, B., Milošević, D., & Manavvi, S. (2021). Review of user-friendly models to improve the urban micro-climate. *Atmosphere, 12*(10). https://doi.org/10.3390/atmos12101291. MDPI.

Johansson, E., Thorsson, S., Emmanuel, R., & Krüger, E. (2014). Instruments and methods in outdoor thermal comfort studies – The need for standardization. *Urban Climate, 10*(P2), 346–366. https://doi.org/10.1016/J.UCLIM.2013.12.002

Juzbašić, A., Ahn, J. B., Cha, D. H., Chang, E. C., & Min, S. K. (2022). Changes in heat stress considering temperature, humidity, and wind over East Asia under RCP8.5 and SSP5-8.5 scenarios. *International Journal of Climatology, 42*(12), 6579–6595. https://doi.org/10.1002/JOC.7636;SUBPAGE:STRING:FULL

Kántor, N., Égerházi, L., & Unger, J. (2012a). Subjective estimation of thermal environment in recreational urban spaces-part 1: Investigations in Szeged, Hungary. *International Journal of Biometeorology, 56*(6), 1075–1088. https://doi.org/10.1007/S00484-012-0523-0/FIGURES/16

Kántor, N., Unger, J., & Gulyás, Á. (2012b). Subjective estimations of thermal environment in recreational urban spaces-part 2: International comparison. *International Journal of Biometeorology, 56*(6), 1089–1101. https://doi.org/10.1007/S00484-012-0564-4/TABLES/8

Konarska, J., Lindberg, F., Larsson, A., Thorsson, S., & Holmer, B. (2014). Transmissivity of solar radiation through crowns of single urban trees-application for outdoor thermal comfort modelling. *Theoretical and Applied Climatology, 117*(3–4), 363–376. https://doi.org/10.1007/s00704-013-1000-3

Krayenhoff, E. S., Broadbent, A. M., Zhao, L., Georgescu, M., Middel, A., Voogt, J. A., Martilli, A., Sailor, D. J., & Erell, E. (2021). Cooling hot cities: A systematic and critical review of the numerical modelling literature. *Environmental Research Letters, 16*(5), Article 053007. https://doi.org/10.1088/1748-9326/ABDCF1

Krüger, E., Emmanuel, R., Drach, P., & Corbella, O. (2012). Comparison of outdoor comfort field data against calculations of the thermal indices PMV and PET. In *Proceedings of 7th Windsor conference: the changing context of comfort in an unpredictable world*. http://nceub.org.uk.

Lam, C. K. C., Gallant, A. J. E., & Tapper, N. J. (2018). Perceptions of thermal comfort in heatwave and non-heatwave conditions in Melbourne, Australia. *Urban Climate, 23*, 204–218. https://doi.org/10.1016/J.UCLIM.2016.08.006

Lau, K. K. L., Lindberg, F., Rayner, D., & Thorsson, S. (2015). The effect of urban geometry on mean radiant temperature under future climate change: A study of three European cities. *International Journal of Biometeorology, 59*(7), 799–814. https://doi.org/10.1007/s00484-014-0898-1

Lau, K. K. L., Tan, Z., Morakinyo, T. E., & Ren, C. (2022). Effects of urban geometry on mean radiant temperature. *SpringerBriefs in Architectural Design and Technology*, 69–83. https://doi.org/10.1007/978-981-16-5245-5_5/FIGURES/8

Lee, H., Mayer, H., & Kuttler, W. (2020). Impact of the spacing between tree crowns on the mitigation of daytime heat stress for pedestrians inside E-W urban street canyons under Central European conditions. *Urban Forestry & Urban Greening, 48*, Article 126558. https://doi.org/10.1016/J.UFUG.2019.126558

Li, X. (2021). Investigating the spatial distribution of resident's outdoor heat exposure across neighborhoods of Philadelphia, Pennsylvania using urban microclimate modeling. *Sustainable Cities and Society, 72*. https://doi.org/10.1016/j.scs.2021.103066

Li, X., & Wang, G. (2021). GPU parallel computing for mapping urban outdoor heat exposure. *Theoretical and Applied Climatology, 145*(3–4), 1101–1111. https://doi.org/10.1007/S00704-021-03692-Z/FIGURES/8

Li, X., Wang, G., Zaitchik, B., Hsu, A., & Chakraborty, T. (2024). Sensitivity and vulnerability to summer heat extremes in major cities of the United States. *Environmental Research Letters, 19*(9), Article 094039. https://doi.org/10.1088/1748-9326/AD6C64

Lin, S., Luo, M., Walker, R. J., Liu, X., Hwang, S. A., & Chinery, R. (2009). Extreme high temperatures and hospital admissions for respiratory and cardiovascular diseases. *Epidemiology (Cambridge, Mass.) (Cambridge, Mass.), 20*(5), 738–746. https://doi.org/10.1097/EDE.0B013E3181AD5522

Linares, C., Díaz, J., Negev, M., Martínez, G. S., Debono, R., & Paz, S. (2020). Impacts of climate change on the public health of the Mediterranean Basin population - current situation, projections, preparedness and adaptation. *Environmental Research, 182*, Article 109107. https://doi.org/10.1016/J.ENVRES.2019.109107

Lindberg, F., & Grimmond, C. S. B (2011). The influence of vegetation and building morphology on shadow patterns and mean radiant temperatures in urban areas: Model development and evaluation. *Theoretical and Applied Climatology, 105*(3), 311–323. https://doi.org/10.1007/S00704-010-0382-8/FIGURES/12

Lindberg, F., Grimmond, C. S. B., Gabey, A., Huang, B., Kent, C. W., Sun, T., Theeuwes, N. E., Järvi, L., Ward, H. C., & Capel-Timms, I. (2018). Urban multi-scale environmental predictor (UMEP): An integrated tool for city-based climate services. *Environmental Modelling & Software, 99*, 70–87.

Lindberg, F., Holmer, B., & Thorsson, S. (2008). SOLWEIG 1.0–Modelling spatial variations of 3D radiant fluxes and mean radiant temperature in complex urban settings. *International Journal of Biometeorology, 52*, 697–713.

Lindberg, F., Onomura, S., & Grimmond, C. S. B. (2016). Influence of ground surface characteristics on the mean radiant temperature in urban areas. *International Journal of Biometeorology, 60*(9), 1439–1452. https://doi.org/10.1007/s00484-016-1135-x

Luo, M., & Lau, N. C. (2021). Increasing human-perceived heat stress risks exacerbated by urbanization in China: A comparative study based on multiple metrics. *Earth's Future, 9*(7), Article e2020EF001848. https://doi.org/10.1029/2020EF001848

Mahdavinejad, M., Shaeri, J., Nezami, A., & Goharian, A. (2024). Comparing universal thermal climate index (UTCI) with selected thermal indices to evaluate outdoor thermal comfort in traditional courtyards with BWh climate. *Urban Climate, 54*, Article 101839. https://doi.org/10.1016/J.UCLIM.2024.101839

Matzarakis, A., Mayer, H., & Iziomon, M. G. (1999). Applications of a universal thermal index: Physiological equivalent temperature. *International Journal of Biometeorology, 43*(2), 76–84. https://doi.org/10.1007/S004840050119/METRICS

Matzarakis, A., Rutz, F., & Mayer, H. (2007). Modelling radiation fluxes in simple and complex environments - application of the RayMan model. *International Journal of Biometeorology, 51*(4), 323–334. https://doi.org/10.1007/s00484-006-0061-8

Matzarakis, A., Rutz, F., & Mayer, H. (2010). Modelling radiation fluxes in simple and complex environments: Basics of the RayMan model. *International Journal of Biometeorology, 54*(2), 131–139. https://doi.org/10.1007/s00484-009-0261-0

Mayer, H., Holst, J., Dostal, P., Imbery, F., & Schindler, D. (2008). Human thermal comfort in summer within an urban street canyon in Central Europe. *Meteorologische Zeitschrift, 17*(3), 241–250. https://doi.org/10.1127/0941-2948/2008/0285

Mohammad, P., Aghlmand, S., Fadaei, A., Gachkar, S., Gachkar, D., & Karimi, A. (2021). Evaluating the role of the albedo of material and vegetation scenarios along the urban street canyon for improving pedestrian thermal comfort outdoors. *Urban Climate, 40*, Article 100993. https://doi.org/10.1016/J.UCLIM.2021.100993

Mutani, G., & Beltramino, S. (2022). Geospatial assessment and modeling of outdoor thermal comfort at urban scale. *International Journal of Heat and Technology, 40*(4), 871–878. https://doi.org/10.18280/IJHT.400402

Nazarian, N., Acero, J. A., & Norford, L. (2019). Outdoor thermal comfort autonomy: Performance metrics for climate-conscious urban design. *Building and Environment, 155*, 145–160. https://doi.org/10.1016/J.BUILDENV.2019.03.028

Nazarian, N., Fan, J., Sin, T., Norford, L., & Kleissl, J. (2017). Predicting outdoor thermal comfort in urban environments: A 3D numerical model for standard effective temperature. *Urban Climate, 20*, 251–267. https://doi.org/10.1016/J.UCLIM.2017.04.011

Ng, E., & Cheng, V. (2012). Urban human thermal comfort in hot and humid Hong Kong. *Energy and Buildings, 55*, 51–65. https://doi.org/10.1016/J.ENBUILD.2011.09.025

Nichol, J. E., & To, P. H. (2012). Temporal characteristics of thermal satellite images for urban heat stress and heat island mapping. *ISPRS Journal of Photogrammetry and Remote Sensing, 74*, 153–162. https://doi.org/10.1016/J.ISPRSJPRS.2012.09.007

Nouri, A. S., Charalampopoulos, I., & Matzarakis, A. (2022). The application of the physiologically equivalent temperature to determine impacts of locally defined extreme heat events within vulnerable dwellings during the 2020 summer in Ankara. *Sustainable Cities and Society, 81*, Article 103833. https://doi.org/10.1016/J.SCS.2022.103833

Obe, O. B., Morakinyo, T. E., & Mills, G. (2024). An assessment of WRF-urban schemes in simulating local meteorology for heat stress analysis in a tropical sub-Saharan African city, Lagos, Nigeria. *International Journal of Biometeorology, 68*, 811–828. https://doi.org/10.1007/S00484-024-02627-3

Oliveira, S., Andrade, H., & Vaz, T. (2011). The cooling effect of green spaces as a contribution to the mitigation of urban heat: A case study in Lisbon. *Building and Environment, 46*(11), 2186–2194. https://doi.org/10.1016/J.BUILDENV.2011.04.034

Palme, M., Privitera, R., & La Rosa, D. (2020). The shading effects of Green infrastructure in private residential areas: Building Performance simulation to support urban planning. *Energy and Buildings, 229*, Article 110531. https://doi.org/10.1016/J.ENBUILD.2020.110531

Pappalardo, S. E., Zanetti, C., & Todeschi, V. (2023). Mapping urban heat islands and heat-related risk during heat waves from a climate justice perspective: A case study in the municipality of Padua (Italy) for inclusive adaptation policies. *Landscape and Urban Planning, 238*, Article 104831. https://doi.org/10.1016/J.LANDURBPLAN.2023.104831

Perkins-Kirkpatrick, S. E., & Lewis, S. C. (2020). Increasing trends in regional heatwaves. *Nature Communications, 11*(1), 1–8. https://doi.org/10.1038/S41467-020-16970-7. SUBJMETA=106,2739,2786,694,704;KWRD=CLIMATE+CHANGE,CLIMATE-CHANGE+IMPACTS,PROJECTION+AND+PREDICTION.

Roudsari, M. S., & Pak, M. (2013). Ladybug: A parametric environmental plugin for grasshopper to help designers create an environmentally-conscious design. *Proceedings of BS 2013: 13th Conference of the International Building Performance Simulation Association, 13*, 3128–3135. https://doi.org/10.26868/25222708.2013.2499

Salamanca, F., Georgescu, M., Mahalov, A., Moustaoui, M., & Wang, M. (2014). Anthropogenic heating of the urban environment due to air conditioning. *Journal of Geophysical Research: Atmospheres, 119*(10), 5949–5965. https://doi.org/10.1002/2013JD021225

Salvati, A., Coch Roura, H., & Cecere, C. (2017). Assessing the urban heat island and its energy impact on residential buildings in Mediterranean climate: Barcelona case study. *Energy and Buildings, 146*, 38–54. https://doi.org/10.1016/J.ENBUILD.2017.04.025

Salvati, A., Kolokotroni, M., Kotopouleas, A., Watkins, R., Giridharan, R., & Nikolopoulou, M. (2022). Impact of reflective materials on urban canyon albedo, outdoor and indoor microclimates. *Building and Environment, 207*, Article 108459. https://doi.org/10.1016/J.BUILDENV.2021.108459

Salvati, A., Monti, P., Coch Roura, H., & Cecere, C. (2019). Climatic performance of urban textures: Analysis tools for a Mediterranean urban context. *Energy and Buildings, 185*, 162–179. https://doi.org/10.1016/J.ENBUILD.2018.12.024

Salvati, A., Palme, M., Chiesa, G., & Kolokotroni, M. (2020). Built form, urban climate and building energy modelling: Case-studies in Rome and Antofagasta. *Journal of Building Performance Simulation, 13*(2), 209–225. https://doi.org/10.1080/19401493.2019.1707876

Schapiro, L. H., McShane, M. A., Marwah, H. K., Callaghan, M. E., & Neudecker, M. L. (2024). Impact of extreme heat and heatwaves on children's health: A scoping review. *The Journal of Climate Change and Health.* , Article 100335. https://doi.org/10.1016/j.joclim.2024.100335

Shashua-Bar, L., Pearlmutter, D., & Erell, E. (2011). The influence of trees and grass on outdoor thermal comfort in a hot-arid environment. *International Journal of Climatology, 31*(10), 1498–1506. https://doi.org/10.1002/JOC.2177

Spagnolo, J., & de Dear, R. (2003). A field study of thermal comfort in outdoor and semi-outdoor environments in subtropical Sydney Australia. *Building and Environment, 38*(5), 721–738. https://doi.org/10.1016/S0360-1323(02)00209-3

Staiger, H., & Matzarakis, A. (2020). Accuracy of mean radiant temperature derived from active and passive radiometry. *Atmosphere, 11*(8), 805. https://doi.org/10.3390/ATMOS11080805. *2020, Vol. 11, Page 805*.

Steemers, K., Baker, N., Crowther, D., Dubiel, J., & Nikolopoulou, M. (1998). Radiation absorption and urban texture. *Building Research & Information, 26*(2), 103–112. https://doi.org/10.1080/096132198370029

Stewart, I. D., & Oke, T. R. (2012). Local climate zones for urban temperature studies. *Bulletin of the American Meteorological Society, 93*(12), 1879–1900. https://doi.org/10.1175/BAMS-D-11-00019.1

Streiling, S., & Matzarakis, A. (2003). Influence of single and small clusters of trees on the bioclimate of a city: A case study. *Journal of Arboriculture, 29*(6), 309–316. https://doi.org/10.48044/JAUF.2003.037

Su, X., Wang, F., Zhou, D., & Zhang, H. (2022). Assessing the spatial variability of daytime/nighttime extreme heat waves in Beijing under different land-use during 2011–2020. *Land, 11*(10), 1786. https://doi.org/10.3390/LAND11101786/S1

Szucs, Á., Gál, T., & Andrade, H. (2014). Comparison of measured and simulated Mean radiant temperature. Case study In Lisbon (Portugal). *Finisterra, 49*(98), 95–111. https://doi.org/10.18055/Finis6469

Tam, B. Y., Gough, W. A., & Mohsin, T. (2015). The impact of urbanization and the urban heat island effect on day to day temperature variation. *Urban Climate, 12*, 1–10. https://doi.org/10.1016/J.UCLIM.2014.12.004

Teitelbaum, E., Alsaad, H., Aviv, D., Kim, A., Voelker, C., Meggers, F., & Pantelic, J. (2022). Addressing a systematic error correcting for free and mixed convection when measuring mean radiant temperature with globe thermometers. *Scientific Reports, 12*(1), 1–18. https://doi.org/10.1038/s41598-022-10172-5. *2022 12:1*.

Thorsson, S., Lindberg, F., Eliasson, I., & Holmer, B. (2007). Different methods for estimating the mean radiant temperature in an outdoor urban setting. *International Journal of Climatology, 27*(14), 1983–1993. https://doi.org/10.1002/JOC.1537

Thorsson, S., Rayner, D., Lindberg, F., Monteiro, A., Katzschner, L., Lau, K. K.-L., Campe, S., Katzschner, A., Konarska, J., & Onomura, S. (2017). Present and projected future mean radiant temperature for three European cities. *International Journal of Biometeorology, 61*, 1531–1543.

Unger, J. (2004). Intra-urban relationship between surface geometry and urban heat island: Review and new approach. *Climate Research, 27*(3), 253–264. https://doi.org/10.3354/CR027253

Vanos, J. K., Rykaczewski, K., Middel, A., Vecellio, D. J., Brown, R. D., & Gillespie, T. J. (2021). Improved methods for estimating mean radiant temperature in hot and sunny outdoor settings. *International Journal of Biometeorology, 65*(6), 967–983. https://doi.org/10.1007/S00484-021-02131-Y/FIGURES/6

Vernon, H. M., & Warner, C. G. (1932). The influence of the humidity of the air on capacity for work at high temperatures. *Epidemiology & Infection, 32*(3), 431–462. https://doi.org/10.1017/S0022172400018167

Villaverde, A., Álvarez, I., Rojí, E., & Garmendia, L. (2024). Categorisation of urban open spaces for heat adaptation: A cluster based approach. *Building and Environment, 263*, Article 111861. https://doi.org/10.1016/J.BUILDENV.2024.111861

Wallenberg, N., Holmer, B., Lindberg, F., & Rayner, D. (2023). An anisotropic parameterization scheme for longwave irradiance and its impact on radiant load in urban outdoor settings. *International Journal of Biometeorology, 67*(4), 633–647. https://doi.org/10.1007/S00484-023-02441-3/FIGURES/8

Wallenberg, N., Lindberg, F., Holmer, B., & Thorsson, S. (2020). The influence of anisotropic diffuse shortwave radiation on mean radiant temperature in outdoor urban environments. *Urban Climate, 31*. https://doi.org/10.1016/j.uclim.2020.100589

Wang, X., Hsu, A., & Chakraborty, T. (2023). Citizen and machine learning-aided high-resolution mapping of urban heat exposure and stress. *Environmental Research: Infrastructure and Sustainability, 3*(3), Article 035003. https://doi.org/10.1088/2634-4505/ACEF57

Weeding, B., Love, P., Beyer, K., Lucieer, A., & Remenyi, T. (2024). High-resolution projections of outdoor thermal stress in the twenty-first century: A Tasmanian case study. *International Journal of Biometeorology, 68*(4), 777–793. https://doi.org/10.1007/S00484-024-02622-8/FIGURES/7

World Health Organization & UN-Habitat. (2016). *Global report on urban health: Equitable healthier cities for sustainable development*.

Yang, X., Yue, W., Xu, H., Wu, J., & He, Y. (2014). Environmental consequences of rapid urbanization in Zhejiang Province, East China. *International Journal of Environmental Research and Public Health, 11*(7), 7045–7059. https://doi.org/10.3390/IJERPH110707045. *2014, Vol. 11, Pages 7045-7059*.